



Multifidelity aerodynamic shape optimization for mitigating dynamic stall using Cokriging regression-based infill

Vishal Raul¹ · Leifur Leifsson^{1,2}

Received: 19 March 2023 / Revised: 13 September 2023 / Accepted: 16 October 2023 / Published online: 6 November 2023
© The Author(s), under exclusive licence to Springer-Verlag GmbH Germany, part of Springer Nature 2023

Abstract

This work proposes a multifidelity modeling approach to mitigate adverse characteristics of airfoil dynamic stall through aerodynamic shape optimization (ASO). Cokriging regression (CKR) is used to efficiently determine an optimum airfoil shape by combining data from high-fidelity (HF) and low-fidelity (LF) computational fluid dynamics simulations. The HF dynamic stall response is modeled using the unsteady Reynolds-averaged Navier–Stokes equations and Menter’s SST turbulence model, whereas the LF model is developed by simplifying the HF model with a coarser discretization and relaxed convergence criteria. The CKR model, constructed using various infill criteria to model the objective and constraint functions with six PARSEC parameters, is utilized to find the optimal design. The results show that the optimal shape from CKR delays the dynamic stall angle over 3° while reducing the peak values of the aerodynamic coefficients compared to the baseline airfoil (NACA 0012). Comparing the optimized shapes from the CKR and a HF Kriging regression (HF-KR) shows a similar delay in dynamic stall angle; however, the CKR optimum provides a better design for the current problem formulation while requiring 39% less computational time than the HF-KR approach. This work presents a new multifidelity modeling approach to saving the computational burden of dynamic stall mitigation through ASO. The approach used in this work is general and can be applied for other unsteady aerodynamic applications and optimization.

Keywords Dynamic stall · Unsteady CFD · Surrogate modeling · Multifidelity modeling · Cokriging regression · Kriging regression

List of symbols

A	Amplitude of oscillations, deg	g	Inequality constraint function
a^s	PARSEC surface coefficient	k_r	Reduced frequency
c	Chord length	m_{max}	Airfoil maximum camber
c_l	Sectional lift coefficient	n	Number of design variables
c_d	Sectional drag coefficient	n_s	Number of design samples
c_m	Sectional pitching moment coefficient	n_t	Number of test data samples
c_{dRE}	Richardson extrapolation estimate of average drag coefficient per cycle, d.c.	PM	Performance metric under consideration
c_{derr}	Estimated error in average drag coefficient, (d.c.)	R_{LE}	Airfoil leading edge radius
d.c.	Drag counts, $\Delta c_d = 0.0001$	Re	Reynolds number
dt	Time-step, sec	t_{off}	Airfoil trailing edge offset
f	Scalar objective function	t_{TE}	Airfoil trailing edge thickness
		t_{max}	Airfoil maximum thickness
		U_∞	Free-stream velocity, m/s
		X	Airfoil surface crest x-coordinate
		x_c	Non-dimensional chordwise location
		$x_{t_{max}}$	Non-dimensional chordwise location of t_{max}
		$x_{m_{max}}$	Non-dimensional chordwise location of m_{max}
		y^+	Non-dimensionalized first layer cell thickness
		Z	Airfoil surface crest z-coordinate
		Z_{xx}	Second-order derivative of airfoil surface
		z_s	Z-coordinate of airfoil section

Responsible Editor: Lei Wang

✉ Leifur Leifsson
leifur@purdue.edu

¹ Department of Aerospace Engineering, Iowa State University, Ames 50011, Iowa, USA

² Purdue University, West Lafayette, USA

\mathbf{x}	Vector of design variables
\mathbf{x}_{lb}	Vector containing lower bounds on design variables
\mathbf{x}_{ub}	Vector containing upper bounds on design variables
α	Angle of attack, deg
α_{ds}	Dynamic stall angle of attack, deg
$\Delta\alpha$	Delay in dynamic stall angle, deg
α_{ms}	Moment stall angle of attack, deg
β_{TE}	Airfoil trailing edge wedge angle, deg
λ	Scalar hyperparameter
ω	Rotational rate, rad/s
θ_{TE}	Airfoil trailing edge directional angle, deg
θ	Vector of Kriging hyperparameters

1 Introduction

An aerodynamic surface experiencing unsteady motion often shows a complex series of events that involves a dynamic delay of stall beyond static stall limits, followed by formation, convection, and shedding of the energetic leading edge vortex, typically described as dynamic stall (Carr 1988). These characteristics of dynamic stall distort the chordwise pressure distribution and produce transient forces and moments much larger than their static counterpart (McCroskey et al. 1976). The dynamic stall phenomenon frequently appears on helicopter rotor blades (Harris and Pruyn 1968), rapidly maneuvering aircraft (Brandon 1991), wind turbines (Buchner et al. 2015), compressor blades (Carr et al. 1977), and bio-inspired micro-air vehicles (Ellington 1999). In many cases, the adverse loading generated by the occurrence of dynamic stall becomes the primary limiting factor in performance, structural strength, and fatigue life of the associated aerodynamic system (Carr 1988; Mani et al. 2012). Thus, mitigating or eliminating dynamic stall over an aerodynamic surface is important for improving performance of aerodynamic systems.

Aerodynamic shape optimization (ASO) provides a cost-effective approach to passively mitigate or delay dynamic stall adverse effects with the utilization of computational fluid dynamics (CFD) for shape evaluation. Although computational evaluation of dynamic stall is costly, surrogate-based optimization (SBO) methods (Forrester et al. 2008) can provide an efficient solution for ASO. The current work proposes the utilization of multifidelity modeling (Peherstorfer et al. 2018; Giselle Fernández-Godino et al. 2019) for delaying and mitigating dynamic stall characteristics through ASO with efficient utilization of computational resources. In fact, current work presents one of the early applications of Cokriging regression (CKR) (Forrester et al. 2007; Kuya et al. 2011) multifidelity model with efficient adaptive sampling strategies to solve complex unsteady dynamic stall mitigation problem. In particular, CKR is implemented to

model the objective and constraint functions with respect to the airfoil shape parameters. The airfoil shape is parameterized using the PARSEC (Rogalsky and Derksen 2009) method. The error-based and expected improvement (EI) infill criteria are utilized to adaptively improve the involved models and efficiently determine optimum design that mitigates adverse effects of dynamic stall. Finally, the constructed surrogate models are utilized for optimization using the multi-start gradient-based method (Peri and Tinti 2012). The optimum design and computational cost from the current approach are compared with the optimum design from a high-fidelity (HF) Kriging regression (KR) surrogate model used in the authors' prior study (Raul and Leifsson 2021). The results of this study provide a detailed analysis of baseline and optimum designs, and provide insight into the impact of airfoil shape on aerodynamic loads and dynamic stall mechanism. The presented approach is general and can be applied to other aerospace systems undergoing dynamic stall.

Next section presents background on the ASO and SBO approaches applied for dynamic stall mitigation studies and other simulation-based design problems. The following section presents the SBO approach utilized in this study including, optimum design problem formulation, design variables, optimization algorithm, surrogate modeling methods, and infill criteria. Then, the CFD model setup is described. The results of the optimization are presented following that. Lastly, the conclusion and suggestions for future work are provided.

2 Background

Significant research has been conducted to understand the dynamic stall and its dependencies in the oscillating pitch cycle. It has long been noted that the dynamic stall is affected by the airfoil motion (Carr et al. 1977) parameters involving the mean angle, amplitude, and frequency of motion. Apart from the motion parameters, the dynamic stall is also affected by parameters describing the airfoil geometry and the operating conditions, such as the Reynolds number and Mach number (Carr et al. 1977; McCroskey et al. 1981). Considering the detrimental effects of dynamic stall, several studies have been conducted to mitigate or control dynamic stall via active-passive systems (Yu et al. 1995; Lee and Gerontakos 2006; Müller-Vahl et al. 2016; Niu et al. 2018; Chandrasekhara et al. 2004; De Giorgi et al. 2020; Zhu et al. 2019).

Unlike active control systems, ASO may provide a cost-effective approach for mitigating or delaying dynamic stall passively without the addition of mass or an auxiliary control system (Wang et al. 2015; Wang and Zhao 2018) and has been widely used for enhancing the performance

of steady-state problems (Mani et al. 2012). However, the application of ASO in a dynamic stall setting could get challenging particularly due to the repetitive evaluations of designs with a computationally costly CFD model, large number of design variables involved with shape parametrization, and gradient computations.

Gradient-based optimization (GBO) is widely used for ASO, utilizing gradient information to locate the local optimum design. Wang et al. (2015) and Wang and Zhao (2018) used sequential quadratic programming algorithm, a GBO method for alleviating dynamic stall characteristics of rotor airfoil. The adjoint method (Jameson 2003) is another approach used for dynamic stall mitigation with ASO (Wong et al. 2006; Nadarajah and Jameson 2007; Mani et al. 2012; Economon et al. 2013) and has shown promising results. The adjoint method is a state-of-art method that provides efficient computation of gradients through adjoint sensitivities and is nearly independent of the number of the design variables (Laurenceau and Meaux 2008), which is particularly advantageous for solving high-dimensional optimization problems. However, the objective function acquired from computational simulations can be non-differentiable, discontinuous, and inherently noisy, making sensitivity information often inaccessible (Koziel and Yang 2011). In case of dynamic stall mitigation using adjoint method, the use of HF simulation model is necessary for accurate computation of sensitivities and to locate optimum design which could get computationally costly. Further, there is a possibility that the conventional adjoint method could fail on chaotic turbulent flow problems such as deep dynamic stall.

SBO (Forrester and Keane 2009; Koziel and Yang 2011) methods have been recognized as being critical in alleviating the computational burden of simulation-based design problems. In the SBO approach, a surrogate model of the objective function is constructed by sparsely sampling the design space with costly HF simulation. The fast to evaluate surrogate is then used for optimization, either with local or global-search optimizers. Surrogate modeling methods consist of data-fit and multifidelity (Peherstorfer et al. 2018) methods. The data-fit methods use the available single-fidelity data (typically HF) to fit a response surface to provide functional relationship between the input variables and output quantities. Polynomial regression (Zhou et al. 2005), Kriging (Simpson et al. 2001), radial basis functions (Forrester et al. 2008), polynomial chaos expansions (Blatman 2009), and support vector regression (Forrester et al. 2008) are some of the widely used data-fit methods used for construction of surrogate models.

In the past, Kriging has been widely used in the performance improvement of rotorcraft and wind turbine airfoils. Kumar and Cesnik (2015) used Kriging with a camber deformation technique for reducing vibratory loads and performance improvement of the rotor in the presence of

dynamic stall. Tang et al. (2017) used Kriging with EI for the performance improvement of a cycloidal rotor. Vu and Lee (2015) and Wang and Zhao (2020) used Kriging for ASO of rotor blades. Yamazaki and Arakawa (2016) utilized Kriging for improving VAWT rotor performance. Veerakumar et al. (2020) used Kriging with experimental wind tunnel evaluations to determine optimum operating parameters of DBD plasma actuator to suppress massive flow separation over a wind turbine airfoil. Recently, the authors investigated the use of KR with EI infill criteria for dynamic stall delay and mitigation over a VAWT airfoil (Raul and Leifsson 2021).

In the SBO approach, an accurate surrogate model is key to finding the global optimum design. Data-fit surrogates generally require higher number of design evaluations for an accurate model construction, thus increasing the computational cost of optimization. The multifidelity modeling could provide further computational cost saving by drawing information from models of multiple fidelities with varying degrees of evaluation speed and accuracy. The multifidelity modeling methods combine data from time-consuming but accurate HF model and fast but less accurate low-fidelity (LF) model to create accurate HF approximations with better generalization capability compared to single-fidelity data-fit surrogates. In multifidelity modeling, typically a greater quantity of LF data is coupled with a small amount of HF data that provides greater accuracy while drastically reducing computational cost (Forrester et al. 2008). Some of the widely used multifidelity techniques are Cokriging (Forrester et al. 2008), space mapping (Koziel et al. 2008; Leifsson and Koziel 2015), and manifold mapping (Echeverría and Hemker 2008; Echeverría 2007).

Forrester et al. (2007) developed the CKR method and applied it to the optimization of a generic transonic civil aircraft wing. Thelen et al. (2020a, b) used Cokriging and CKR for predicting aeroelastic flutter of airfoils and wings. Kuya et al. (2011) utilized CKR with experimental and computational dataset for modeling an inverted wing with vortex generators in ground effect. Nagawkar et al. (2021) used manifold mapping for single- and multi-point design optimization of transonic airfoils. Koziel et al. (2008) used space mapping for design optimization and modeling of microwave circuit. More recently, Bailly and Bailly (2019) applied Kriging and Cokriging with EI infill strategy for the design of rotor blade performance improvement in forward flight. They showed that Cokriging was able to provide more realistic results compared to Kriging with lower consumption of HF samples. However, the multifidelity modeling methods have received limited attention for ASO-based dynamic stall mitigation. In this work, CKR with error-based and EI infill criteria is applied for efficient ASO of airfoils at low Reynolds and Mach numbers to mitigate dynamic stall.

3 Surrogate-based shape optimization

This section presents the proposed ASO method for delaying dynamic stall with surrogate modeling. First, the optimum design problem formulation, design variables, and optimization algorithm used in the current study are described. Finally, the surrogate modeling methods are described in detail along with the error-based and EI-based infill criteria.

3.1 Optimum design problem formulation

Typically, the dynamic stall phenomenon is studied using a sinusoidally oscillating airfoil in free-stream flow. The oscillating motion of an airfoil can be given as

$$\alpha(t) = \alpha_m + A \sin(\omega t), \tag{1}$$

where A , ω and α_m denote the pitching amplitude, the rotational rate, and the mean angle of attack, respectively. Reduced frequency is another important parameter that affects the characteristics of dynamic stall and is defined as

$$k_r = \frac{\omega c}{2U_\infty}, \tag{2}$$

where U_∞ is the free-stream speed and c is the airfoil chord length. For this study, a deep dynamic stall case from the experimental work conducted by Lee and Gerontakos (2004) is employed for the ASO application. The motion and flow parameters of the selected case are $\alpha_m = 10^\circ$, $A = 15^\circ$, $k_r = 0.05$, $\omega = 3.403$, and a Reynolds number $Re = 135,000$.

The primary objective of this study is to determine the airfoil shape that delays the occurrence of the dynamic stall while mitigating the adverse dynamic loading of the airfoil. This objective can be achieved by delaying or eliminating the dynamic stall vortex (DSV) formation over the airfoil (suction side), which is predominantly responsible for sudden changes in the aerodynamic forces and moments. The DSV occurrence over an airfoil surface can be located by divergence in drag and pitching moments coefficients. Thus, the DSV formation can be delayed or eliminated by the following optimization problem formulation given as

$$\min_{\mathbf{x}} f(\mathbf{x}) = \left(\frac{\sum_{i=1}^N c_{d_i}(\mathbf{x})}{J(c_{d0})} \right) + \left(\frac{\sum_{i=1}^N |c_{m_i}(\mathbf{x})|}{J(c_{m0})} \right) \tag{3}$$

$$s.t. \quad g(\mathbf{x}) = \alpha_{ds0} + \Delta\alpha - \alpha_{ds}(\mathbf{x}) \leq 0 \tag{4}$$

$$\mathbf{x}_{lb} \leq \mathbf{x} \leq \mathbf{x}_{ub}, \tag{5}$$

where $J(c_{d0}) = \sum_{i=1}^N (c_{d0})_i$, $J(c_{m0}) = \sum_{i=1}^N |(c_{m0})_i|$, and $\mathbf{x} = [x_1, x_2, \dots, x_n]^T$ is the design variable vector of n dimensions with \mathbf{x}_{lb} and \mathbf{x}_{ub} as the lower and upper bounds of \mathbf{x} , respectively. The subscript ‘0’ represents properties

of baseline airfoil shape (NACA 0012). The parameters $c_d(\mathbf{x})$, $c_m(\mathbf{x})$, and $\alpha_{ds}(\mathbf{x})$ represent time variant drag coefficient, pitching moment coefficient, and dynamic stall angle of the airfoil shape, respectively. The parameter N denotes the number of time-steps in each pitching cycle and the magnitude of N depends on the simulation time-step and the total cycle time. The constraint function (4) forces the optimal design to delay the dynamic stall angle by $\Delta\alpha$ over the baseline design (α_{ds0}), which is the minimum delay in dynamic stall angle expected from the optimum design. In this study, only the upstroke part of the pitching cycle is considered, where the formation of the DSV primarily affects the aerodynamic forces and moments, and to utilize minimal computational resources.

3.2 Design variables

In this work, the PARSEC (Sobieczky 1999) airfoil parameterization method is used to define the airfoil shape. The PARSEC method parameterizes an airfoil by using a set of variables that have a specific meaning related to the airfoil’s surface, such as the leading edge radius, the trailing edge wedge angle, and the thickness (Rogalsky and Derksen 2009). Design variables with a specific meaning are desirable to designers for an improved understanding of dynamic stall characteristics and their dependence on the airfoil features.

PARSEC parameterizes an airfoil by its upper and lower surface curves given as Rogalsky and Derksen (2009); Sobieczky (1999)

$$z_s = \sum_{i=0}^6 a_i^s x_c^{i-\frac{1}{2}}, \quad s = U, L \tag{6}$$

where z_U and z_L are the height of upper and lower surface curves in z-coordinates, x_c is the non-dimensional distance along chord, and a_i^s are the coefficients to be determined. Figure 1 and Table 1 show the shape parameters used in PARSEC. A total of twelve parameters define the entire airfoil shape, where each surface (upper and lower) is defined

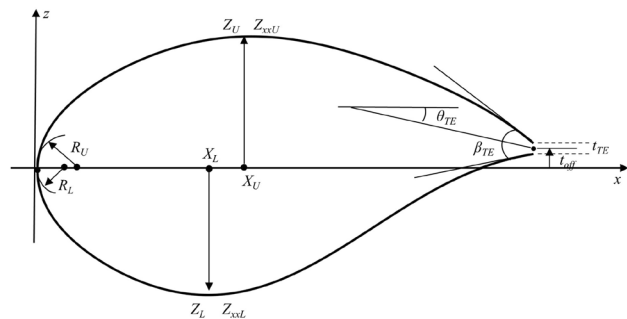


Fig. 1 PARSEC airfoil geometry parametrization

Table 1 Design variables in PARSEC airfoil parameterization

Design variable	Description	Units
X	Surface crest x-coordinate	–
Z	Surface crest z-coordinate	–
Z_{xx}	Second-order derivative at X, $\frac{d^2z}{dx^2} _{x=X}$	–
R_{LE}	Leading edge radius	–
θ_{TE}	Trailing edge directional angle	Deg
β_{TE}	TE wedge angle	Deg
t_{off}	Trailing edge offset	–
t_{TE}	Trailing edge thickness	–

using parameters shown in Table 1. The last four parameters shown in Table 1 are the common parameters between upper and lower airfoil surfaces. The PARSEC parameterization has twelve parameters in twelve equations that are solved to determine the coefficients a_i^S .

The predominant feature of dynamic stall is formation, growth, and convection of DSV that occurs on the suction side or upper surface of an airfoil. Mitigation of dynamic stall can be achieved by delaying or eliminating the formation of DSV. The DSV formation is affected by leading edge curvature (Yu et al. 1995; Müller-Vahl et al. 2016; Wang and Zhao 2020), pressure gradient on suction side (Chandrasekhara et al. 2004), airfoil thickness (Sharma and Visbal 2019), and camber (Müller-Vahl et al. 2016). These factors can be effectively controlled by variation in airfoil upper surface with minimal design parameters. Thus, in this work, the parameters that primarily affect the airfoil upper surface are considered. The upper and lower surface leading edge radius is represented by a single variable ($R_{LE} = R_U = R_L$) to consider the impact of leading edge radius on the dynamic stall characteristics. Additionally, the trailing edge offset (t_{off}) and trailing edge thickness (t_{TE}) parameters are set to zero to keep the number of design variables that predominantly affect dynamic stall to a minimum and to reduce the complexity during the meshing operations.

The conditions mentioned above reduce the twelve design variables to six design variables producing a unit length airfoil with a sharp trailing edge. Here, the design variable vector is written as

$$\mathbf{x} = [X_U, Z_U, Z_{xx_U}, R_{LE}, \theta_{TE_U}, \beta_{TE_U}]^T, \tag{7}$$

where the bounds on the design variables are presented in Table 2. The variable bounds are selected to provide a large variation in airfoil shapes without producing atypical shapes.

3.3 Optimization algorithm

The optimization algorithm presented in this study is an automated loop that sequentially improves the search of

Table 2 Design variable bounds

Design variable	Lower bound	Upper bound	Units
X_U	0.2733	0.5011	–
Z_U	0.054	0.09	–
Z_{xx_U}	– 0.6726	– 0.4036	–
R_{LE}	0.0104	0.0222	–
θ_{TE_U}	– 11.7156	– 7.0294	Deg
β_{TE_U}	3.52818	5.8803	Deg

global optimum using the multifidelity Cokriging surrogate model. In a multifidelity model, LF data are exploited to represent a global trend of a true function and provide a base for HF approximation (Kuya et al. 2011). Thus, the accuracy of the multifidelity surrogate model could highly depend on the global accuracy of the LF surrogate model (Kuya et al. 2011) which in turn depends on the LF sampling plan that is distributed in design space properly. Therefore, the proposed optimization algorithm is implemented in two parts. The purpose of the first part is to determine an appropriate LF sampling plan that captures the global trend (see Fig. 2). First, the LF Kriging regression (LF-KR) model is constructed and refined sequentially using an error-based infill (cf. Sect. 3.5) strategy. The error-based infill strategy is typically used to achieve globally accurate surrogate. This process determines the appropriate number of LF samples required for getting globally accurate LF surrogate. Once the appropriate number of LF samples is determined, initial CKR model is constructed with acquired LF samples (from the first part of algorithm) and initial HF samples. The CKR

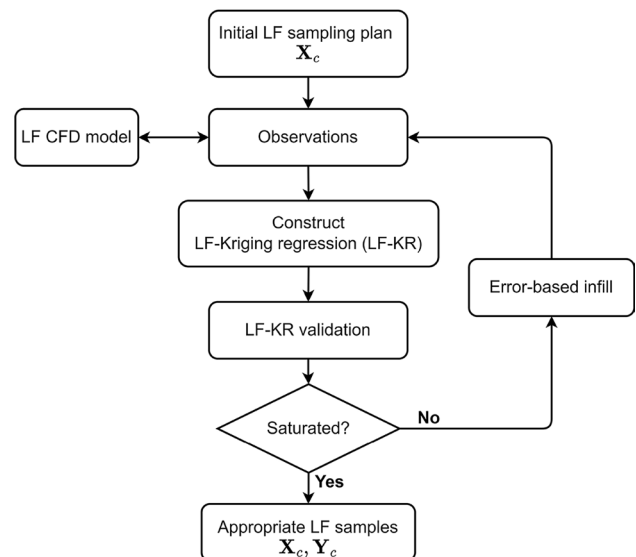


Fig. 2 A flowchart of the first part of optimization algorithm to determine an appropriate LF sampling plan that captures the global trend in the underlying function

model is then further refined by using EI infill strategy (cf. Sect. 3.5). EI infill strategy is a balanced exploration–exploitation strategy that is typically used to find global optimum efficiently. This two-step approach allows to efficiently build Cokriging surrogate.

A flowchart of the first part of algorithm to determine the LF sampling plan is shown in Fig. 2. The algorithm starts by sampling the design space using the Latin hypercube sampling (LHS) (McKay et al. 2000) method. The samples \mathbf{X}_c are generated such that $\mathbf{X}_e \subset \mathbf{X}_c$ (cf. Sect. 3.3.1), where \mathbf{X}_c and \mathbf{X}_e are LF and HF sampling plans and subscripts ‘e’ and ‘c’ denote expensive and cheap to evaluate models, respectively. Next, the samples \mathbf{X}_c are evaluated with the LF CFD model. The observations are then used to construct two separate LF-KR models, one for the objective and another for the constraint function. The global accuracy of the LF-KR models is evaluated against the test data set using the NRMSE (normalized root mean square) metric. An error-based infill strategy is implemented on the objective function surrogate to determine the infill (cf. Sect. 3.5). Next, the infill point is evaluated with the LF CFD model and added to the initial sampling plan \mathbf{X}_c . In every infill iteration, the LF-KR model is checked for saturation, i.e., when the global accuracy of the LF-KR surrogate will not improve with an additional infill point. Once the LF-KR model is saturated, the first part of the algorithm terminates to provide a sampling plan \mathbf{X}_c holding infill as well as the initial samples and the corresponding LF observations \mathbf{Y}_c that produces a globally accurate LF surrogate model.

A second part of the algorithm to find the optimal design is shown in Fig. 3. The HF data are generated by evaluating the HF CFD model at \mathbf{X}_e . The LF data \mathbf{X}_c acquired from the first part along with HF data \mathbf{X}_e are used to construct two separate CKR models, one for objective and the other for constraint function. The constructed CKR models are then used to solve the optimization problem (3, 4) considered in this study and acquire optimal design in every iteration. Next, the termination conditions are checked. If the required termination criteria are not satisfied, an infill point is determined using an EI-based infill strategy. The infill point is evaluated with LF and HF CFD models and added to their respective data sets. The above process continues until the convergence in maximum EI magnitude and consecutive optimal shapes are achieved. After the satisfaction of termination criteria, the final optimal design is evaluated with HF CFD model for further comparison with baseline design.

3.3.1 Sampling plan

The surrogate model is data-driven and its accuracy depends on the appropriate sampling plan. It is important to capture the trend of the objective function over the entire design domain. In this study, the LHS method is used, which

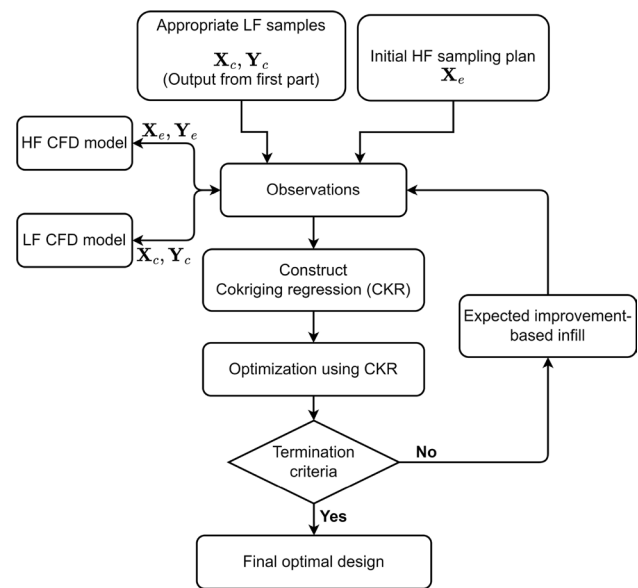


Fig. 3 A flowchart of the second part of optimization algorithm to find the optimal design using Cokriging regression with EI-based infill

provides a good distribution of sample points over the entire design domain, ensuring the full range of the design variables is represented. The LHS method is used for generating training and testing data sets for this study. The training data sets satisfy the $\mathbf{X}_e \subset \mathbf{X}_c$ condition. This condition is satisfied by generating two LHS plans. Both plans are combined to provide initial LF sampling plan \mathbf{X}_c , whereas only one of the plans (typically of smaller size) is used as the HF sampling. For this study, the LHS plans are generated using the pyDOE2 python package (Sjögren and Svensson 2021).

Another critical part of the sampling plan is the selection of the number of samples. According to Gu and Yang (2006) and Shi et al. (2012), a number of samples equal to 3 times the number of design variables are needed at a minimum for the construction of a reasonably accurate surrogate model. For this study, the airfoil shape is represented by six design variables. Thus, to keep the number of HF evaluation to a minimum, approximately, 3 times the number of design variables is set as the number of HF samples, and the number of LF samples is set to be approximately 10 times the number of HF samples (Forrester et al. 2008).

3.4 Surrogate modeling

Simulation-based engineering objective functions are, in general, inherently noisy. In the case of physical experiments, the data used could involve noise from many factors beyond the control of experimentation. The computer experiments are deterministic, producing the same output for the same input. However, computer experiments,

such as CFD, that are based on the simulation of physical phenomena using iterative and discretized schemes may produce similar characteristics in data as physical experiments (Forrester et al. 2006). Identical computer experiments will produce the same results; however, the immediately adjacent inputs may produce entirely different results due to discretization error and rate of convergence, making results of computer experiments appear to contain noise (Forrester et al. 2006). The discretization error is mainly caused by finite changes in mesh due to small geometric changes, whereas convergence impacts data noise if the simulations for different inputs converged at different rates. Thus, functions formulated from computational simulations, such as CFD, could also exhibit noise. Additionally, in case of dynamic stall simulation, the objective function value may get affected by the chaotic nature of deep dynamics of stall adding noise into objective and constraint functions. In the current study, the objective and constraint function is expected to exhibit noise. If such data are not handled correctly during surrogate model construction, it could lead to numerical instability and generation of pseudo optimums in the design space, prolonging the global optimum search process. Thus, it is critical to use a surrogate that can handle noisy data to enable a robust estimation of the optimal design.

In this work, CKR (Forrester et al. 2007) is used to model the objective and constraint function over the entire design space. Cokriging (Forrester et al. 2007) is a multi-response extension of Kriging that combines data of different fidelities. The Cokriging description given here assumes two fidelity levels (Forrester et al. 2007, 2008), the HF response \mathbf{y}_e at $\mathbf{X}_e = [\mathbf{x}_e^1, \mathbf{x}_e^2, \dots, \mathbf{x}_e^{n_e}]^T$ and the LF response \mathbf{y}_c at $\mathbf{X}_c = [\mathbf{x}_c^1, \mathbf{x}_c^2, \dots, \mathbf{x}_c^{n_c}]^T$, where $(\mathbf{X}_e \subset \mathbf{X}_c)$. The Cokriging model is constructed in two steps. First, a LF Kriging model $\hat{y}_c(\mathbf{x})$ is fitted to the LF sample response \mathbf{y}_c where the first set of hyperparameters, $\boldsymbol{\theta}_c$, is obtained. Next, the difference Kriging model $\hat{y}_d(\mathbf{x})$ is fitted to $\mathbf{y}_d = \mathbf{y}_e - \rho\hat{y}_c(\mathbf{X}_e)$ at \mathbf{X}_e to obtain the second set of hyperparameters, $\boldsymbol{\theta}_d$ and ρ . The scaling hyperparameter ρ in the difference model scales the LF approximations to the HF response. All the hyperparameters are determined using the Maximum likelihood estimate function during the fitting process.

CKR is a version of Cokriging developed to filter noise from the HF and LF data sets. The noise filtering capability of CKR is obtained by introducing regression constants in LF and difference Kriging models (Forrester et al. 2007, 2006). These two additional hyperparameters are also tuned during the fitting process. The detailed explanation of Kriging, Cokriging, and CKR can be found in Forrester et al. (2008, 2007); Raul and Leifsson (2021); Thelen et al. (2020a).

3.5 Infill criteria

The surrogate model is constructed based on a limited observed response in a given design space, and it is only an approximation of the true function. The optimum design depends on the accuracy of the surrogate model. Therefore, it is desirable to improve the accuracy of the surrogate model with further evaluations (infill points), in addition to the initial sampling plan. A surrogate model can employ an infill strategy with pure exploration, pure exploitation, or a combination of both (Thelen et al. 2020a). The pure exploration strategy is generally used to improve the global accuracy of the model, while pure exploitation is used to find optimum quickly by adding infill points near the current minima in every infill iteration. In case of pure exploitation, the global accuracy of the model may not improve as most of the infill samples are placed near the current optimum. A balanced exploitation and exploration infill strategy combines the favorable features of both by providing an improved global accuracy as well as the faster prediction of global optimum.

An error-based infill criterion is a pure exploration strategy where a new infill point is added wherever the model uncertainty is largest. The Kriging-based surrogate model provides model uncertainty through estimation of mean square error (MSE) (Forrester et al. 2008, 2007). The infill point can be determined by maximizing the MSE function of the surrogate model with a global optimizer. For this study, a differential evolution optimizer is used for finding the infill point based on MSE.

An error-based infill strategy is used in this work to determine an appropriate number of LF samples by improving the global accuracy of the LF surrogate model. Typically, a stopping criterion based on the saturation of the surrogate model is used (Forrester et al. 2008) with error-based infill strategy, i.e., when any further addition of infill points does not improve the surrogate model. The determination of the saturation condition can be based on the NRMSE that provides a metric for quantifying global accuracy of the surrogate model.

In this study, the global accuracy of the LF surrogate model is quantified by the NRMSE metric and it is defined as

$$\text{NRMSE} = \frac{\sqrt{\sum_{i=1}^{n_t} \frac{(y_i^j - \hat{y}_i^j)^2}{n_t}}}{(y_{\max} - y_{\min})_t}, \quad (8)$$

where y_i^j and \hat{y}_i^j represent the responses ($f(\mathbf{x})$ or $g(\mathbf{x})$) from the LF CFD model evaluation and LF-KR model prediction at the i^{th} test sample, respectively. The n_t represents the number of test data samples. The denominator of (8), $(y_{\max} - y_{\min})_t$, represents the difference between the maximum and minimum responses from the test data samples that is separately

generated using the LHS sampling plan and evaluated using the LF CFD model. A total of 20 test data points are generated for validation of the LF-KR model.

If the NRMSE metric between successive surrogates plateaus, then it can be assumed that further addition of an error-based infill will not improve the model. In this study, a weighted moving average (WMA) of the NRMSE with a window size of five is used to determine when the LF surrogate model is saturated. The WMA computation used in this study is given as

$$PM_{WMA} = \frac{PM_i w_1 + PM_{i-1} w_2 + \dots + PM_{i-5} w_5}{w_1 + w_2 + \dots + w_5}, \tag{9}$$

where PM_i is the performance metric used at the i^{th} infill iteration with weights $[w_1, w_2, w_3, w_4, w_5] = [5, 4, 3, 2, 1]$. In this study, the modeling of a LF surrogate is considered to be saturated if the difference between successive $NRMSE_{WMA}$ values is less than 10^{-5} i.e., $NRMSE_{WMA}^{(i)} - NRMSE_{WMA}^{(i-1)} \leq 10^{-5}$.

EI (Forrester et al. 2008) is a well-known infill strategy that provides a balanced exploitation and exploration of the objective function and can be written as Forrester et al. (2008)

$$\mathbb{E}[I(\mathbf{x})] = \begin{cases} (y_{\min} - \hat{y}) \Phi\left(\frac{y_{\min} - \hat{y}}{\hat{s}}\right) + \hat{s} \phi\left(\frac{y_{\min} - \hat{y}}{\hat{s}}\right) & \text{when } \hat{s} > 0 \\ 0 & \text{when } \hat{s} = 0 \end{cases} \tag{10}$$

where Φ and ϕ are the cumulative distribution function and the probability density function, respectively. The EI computation can be implemented as Forrester et al. (2008)

$$\mathbb{E}[I(\mathbf{x})] = (y_{\min} - \hat{y}) \left[\frac{1}{2} + \frac{1}{2} \operatorname{erf}\left(\frac{y_{\min} - \hat{y}}{\hat{s}\sqrt{2}}\right) \right] + \hat{s} \frac{1}{2\pi} \exp\left[-\frac{(y_{\min} - \hat{y})^2}{\hat{s}^2}\right], \tag{11}$$

where ‘erf’ is the error function defined as

$$\operatorname{erf}(z) = \frac{2}{\sqrt{\pi}} \int_0^z e^{-t^2} dt. \tag{12}$$

The infill point for a trained surrogate model can be determined by maximizing the EI (11) using a global optimizer, such as differential evolution. Kriging and Cokriging can be directly used with EI for infill point determination as $\hat{s} = 0$ and $\mathbb{E}[I(\mathbf{x}_\mu)] = 0$ at already sampled sites, which avoids resampling, thereby assuring global convergence of the infill process (Forrester et al. 2008). However, KR and CKR surrogate models should not be directly used with the EI approach due to the possibility of resampling at observed locations, as the error \hat{s} is always present in regression models, halting the convergence (Forrester et al. 2008, 2007). In such case, resampling is avoided by redefining the error

estimation using re-interpolation (Forrester et al. 2008, 2006, 2007) which reduces error at already sampled locations to zero ($\hat{s} = 0 \Rightarrow \mathbb{E}[I(\mathbf{x})] = 0$), allowing the EI-based infill criteria regain its global convergence property. In this work, EI-based infill is used with CKR model to efficiently locate global optimum.

Convergence of the EI-based infill approach is usually determined based on the magnitude of expected improvement (Forrester et al. 2008). Typically, a very low value of $\mathbb{E}[I(\mathbf{x})]$ is selected as a stopping criteria indicating that the expectation of model improvement is low. However, care should be taken to make sure that the $\mathbb{E}[I(\mathbf{x})]$ values are consistently lower. For this study, WMA of the maximum EI magnitude, i.e., $\max(\mathbb{E}[I(\mathbf{x})])_{WMA} \leq 10^{-4}$, along with convergence in consecutive optimal designs, is used as the termination criteria of the EI-based infill process.

4 Computational fluid dynamics modeling

This section presents the CFD setup used in the current study for dynamic stall evaluation of airfoil shapes. Initially, flow solver description and its setup is presented followed by the details of computational grid generation and the results of the grid and time independence studies are presented. Further, HF CFD model validation and the construction of low-fidelity model are described.

4.1 Flow solver

In the current study, fluid flow simulations are performed with the Stanford University Unstructured (SU2) (Palacios et al. 2013, 2014) an open-source CFD software. The dynamic stall simulation is performed by solving the unsteady compressible Reynolds-Averaged Navier–Stokes (RANS) equations with Menter’s shear stress transport (SST) (Menter 1994) turbulence model using an implicit solver. In the past, Menter’s SST model has shown an acceptable level of performance in dynamic stall simulations to capture the formation, convection, and shedding of DSV (Wang et al. 2010; Hand et al. 2017; Daróczy et al. 2015).

The dynamic stall simulation performed in this study utilizes second-order dual-time stepping (Palacios et al. 2013) and rigid grid motion (Economou et al. 2013). The governing equations are discretized using a finite volume method with convective flux for the mean flow equations is computed using the Jameson-Schmidt-Turkel scheme, the turbulence working variables for Menter’s SST model are convected using a first-order scalar upwind method, and the viscous flux computations of the flow variable gradients are done with the Green-Gauss method, and the maximum Courant-Friedrichs-Lewy number is selected as 4. For unsteady flow, SU2 suggests a second-order dual-time-stepping strategy to

achieve high-order accuracy in time (Palacios et al. 2013; Economon et al. 2016, 2013). In this method, the unsteady problem is converted into a series of steady problems at each physical time-step, which is then solved consecutively with steady-state convergence acceleration techniques. As a result, there are 2 time iterators. The inner (pseudo time) iterator and the outer (physical time) iterator. For this study, the inner iteration utilizes Euler implicit scheme (Palacios et al. 2013) with internal iterations set to 2,400 and outer iteration employs second-order BDF scheme. Further, the two-level multigrid W-cycle method is implemented for convergence acceleration. The Cauchy convergence criteria (Abbott 2001) are utilized on the drag computation with Cauchy-epsilon criteria of 10^{-6} over 100 iterations.

4.2 Grid generation

In this study, computational grids are generated using the blockMesh utility offered by OpenFOAM (OpenFOAM 2021) that generates meshes by decomposing the domain geometry in sets of three-dimensional hexahedral blocks. For the current dynamic stall simulation, a C-grid topology is used with a radius of 55 chord lengths from the airfoil leading edge and a downstream distance of 62 chord lengths. The mesh is highly refined near the airfoil surface with $y^+ \leq 0.8$ and the growth ratio of 1.05 normal to the airfoil surface. The mesh refinement with a low y^+ value is necessary to capture the onset of dynamic stall vortex and complex flow physics generated during the dynamic stall cycle. The airfoil surface is modeled as a no-slip adiabatic wall, whereas the domain boundary is set as farfield boundary condition with Reynolds number of 135,000 and Mach number of 0.1. The pitching motion is generated with rigid grid motion, where mean angle of attack, amplitude, and rotation rate are selected based on selected test case (see Sect. 3.1). A similar grid topology is used to generate

additional meshes to perform a grid convergence study, as discussed in the next section. The generated mesh using the blockMesh utility is converted to a SU² compatible file format to use with SU² solver. Figure 4 shows views of a coarse computational mesh used for the NACA 0012 airfoil.

4.3 Grid and time independence studies

The grid and time independence study is conducted to provide an appropriate selection of spatial and temporal resolution for the unsteady simulation that accurately captures the dynamic stall characteristics and flow physics. The grid and time independence study is conducted in two steps. First, the spatial resolution of the grid is determined by performing a grid study with a steady-state simulation at a fixed angle of attack. The resulting grid is then used in unsteady simulation with a pitching cycle to identify an appropriate time-step. There is a possibility that the spatial resolution of the grid may not be adequate for an unsteady simulation. However, we have taken excessive care to refine the mesh near airfoil surface by keeping $y^+ \leq 0.8$ and the growth ratio of 1.05 normal to the airfoil surface which provides sufficient resolution for an unsteady simulation.

The grid study is performed on the baseline airfoil (NACA 0012) at $Re = 135,000$, angle of attack 4° , turbulence intensity of 0.08%, and the Cauchy convergence criteria set on the drag values (Cauchy-epsilon value of 10^{-6}) with a RANS solver provided by SU2. A total of five grids with ascending spatial resolution are generated by increasing the number of cells in normal, chordwise, and downstream directions, producing the finest grid of 720,000 cells and the coarsest grid of 157,250 cells as shown in Table 3. The three grids with the highest spatial resolutions show a minimal variation of $\Delta c_l \leq 0.003$ in their lift coefficients with drag coefficient varying within under 4 d.c. Further, the simulation time for grid 3 is approximately one-third of the finest

Fig. 4 Computational domain with a coarse C-grid around the baseline airfoil (NACA 0012) and a zoomed in view of the airfoil

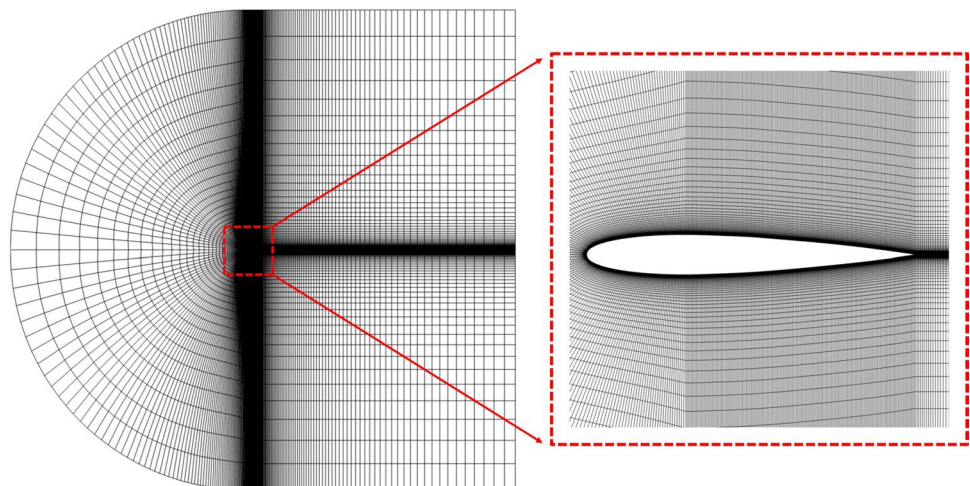


Table 3 Grid convergence study on the baseline design

Grid	Number of elements	Lift	Drag (d.c.)	Simulation time* (min)
1	159,250	0.385	126.8	15
2	259,200	0.395	174.3	75
3	387,200	0.414	180.4	146
4	540,800	0.416	184.7	220
5	720,000	0.417	184.2	298

*Computed on a high-performance cluster with 64 processor cores. Wall-clock time

Table 4 Results of the time-step independence study with the baseline airfoil NACA 0012

dt (sec)	$c_{d_{avg}}$ (d.c./cycle)	Simulation time* (hrs/cycle)	$c_{d_{err}} = c_{d_{avg}} - c_{d_{RE}} $ (d.c.)
0.008	1,813	39	294.5
0.004	2,019	51	88.4
0.002	2,093	65	14.9
0.0015	2,103	69	4.8
0.0010	2,105	78	2.1

*Computed on a high-performance cluster with 112 processor cores. Wall-clock time

grid. Thus, grid 3 with 387,200 cells is selected for all HF investigations conducted in this study.

The selected spatial resolution from the grid study is used for determining the physical time-step for accurate unsteady simulation. The time study is done using the generalized Richardson extrapolation method (Roy 2003) on the average drag coefficient per oscillating cycle $c_{d_{avg}}$ metric. The Richardson extrapolation provides an estimate of performance metric at higher order using the low-order data. Multiple unsteady simulations with descending time-steps are conducted as shown in Table 4. These low-order values are used to provide Richardson extrapolation estimate $c_{d_{RE}}$ of 2,108 d.c. Table 4 shows the estimated error $c_{d_{err}}$ from $c_{d_{RE}}$ and the simulation time at respective time-steps (dt). A time-step of 0.0015 sec is selected based on error $c_{d_{err}} \leq 5$ d.c metric with a lowest possible simulation time.

4.4 High-fidelity CFD model validation

The current CFD setup with selected grid and time-step is validated against the experimental (Lee and Gerontakos 2004) and Large eddy simulation (LES) results (Kim and Xie 2016) at a considered dynamic stall test case and is shown in Fig. 5. The LES results shown here are averaged over three cycles, whereas the experimental results

are averaged over hundred cycles. The CFD setup with the selected grid and time-step is considered as an HF simulation model to evaluate the dynamic stall response of airfoils. For the validation of the HF CFD model, the dynamic stall simulation at the considered test case is performed over 1.25 cycles where airfoil initially starts from a mean angle of attack (10°) and pitch in downstroke cycle. Once the airfoil reaches the lowest angle (-5°), the data are collected for the next complete cycle. It is observed that the addition of the initial downstroke part of the cycle helps stabilize the flow from the abrupt change in rotational rate from zero to a finite value at the first time-step. Additionally, it is observed that after the initial quarter downstroke cycle, additional simulation over multiple pitching cycles produces a minimal variation in aerodynamic responses. Thus, for this study, all dynamic stall simulations are started with a quarter downstroke pitching cycle, and data are gathered for the remaining part of the pitching cycle. A detailed discussion on HF CFD model validation can be found in Raul and Leifsson (2021).

From Fig. 5, it is noted that the HF URANS model shows a reasonable agreement with LES model and shows a qualitative agreement with experimental results. The dynamic stall and moment stall location from these approaches are shown in Table 5. It is observed that the HF URANS model was able to capture global features of dynamic stall mechanism such as the moment stall, generation, growth, convection and progression of the DSV, massive flow separation after DSV detachment, and finally the flow reattachment. The HF URANS model captures the moment stall (at 16.6°) and dynamic stall (at 19.2°) locations early in the oscillation cycle (Table 5) while over-predicting peak lift, drag, and pitching moment coefficient magnitudes (Fig. 5). The HF URANS model shows a good agreement with LES in the upstroke cycle (-5° to 25°), whereas in the downstroke cycle (25° to -5°), where massive flow separation is expected, the HF URANS model shows limited compliance with LES and experimental results.

Overall, from the validation process, it is observed that the LES model demonstrates much closer agreement with experimental results than the HF CFD model used in the current study, making it an ideal model to use in ASO for dynamic stall simulation. However, the computational cost of a single LES evaluation is substantially higher than URANS and using LES for optimization studies is currently impractical. Considering the requirement of multiple evaluations in the optimization process currently URANS model provides a practical option for evaluating dynamic stall over airfoils and thus used in the current study. That said, with rapid developments in LES methodology and advance in computational power, LES simulations may become practical in future for optimization studies. In that case, LES

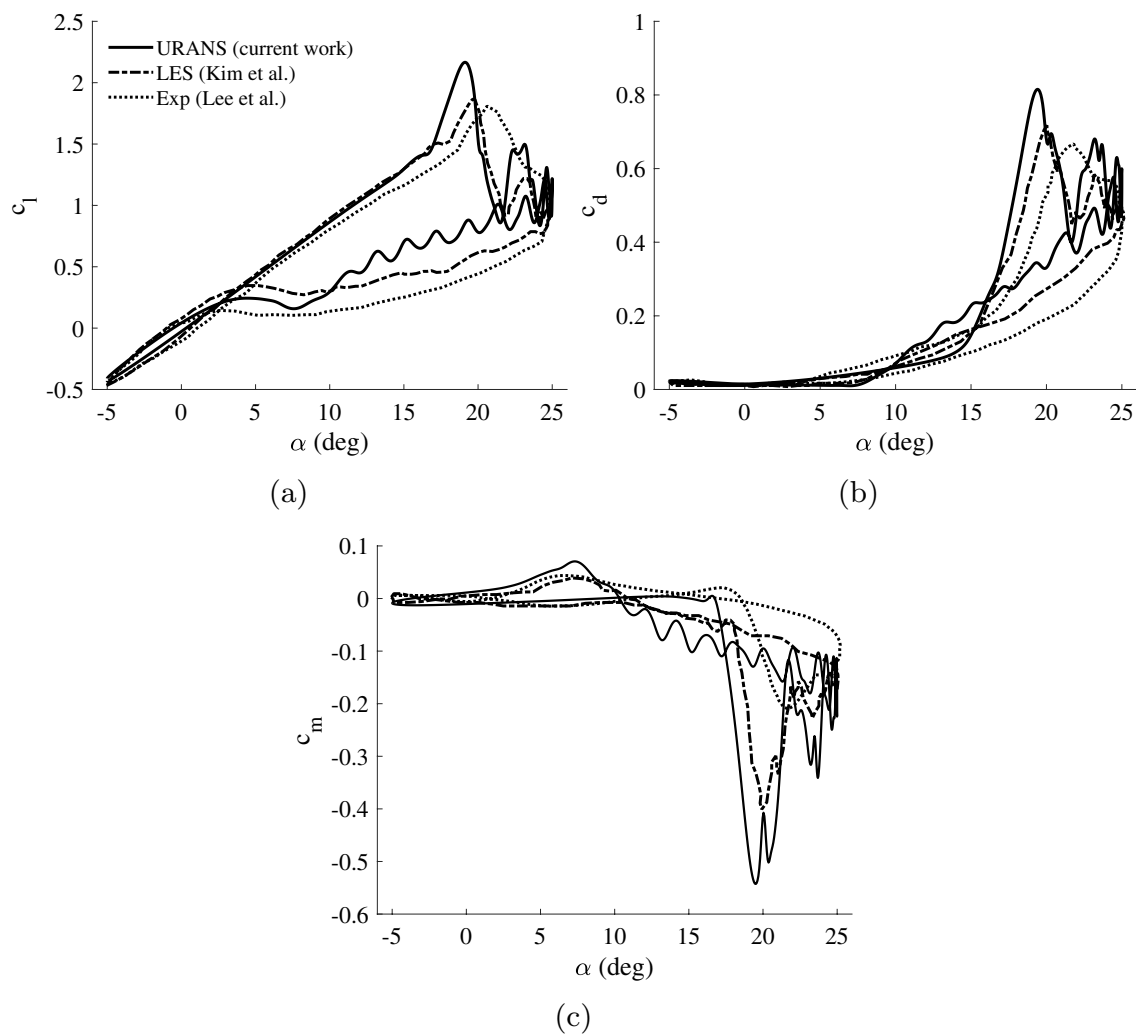


Fig. 5 A comparison of the time-dependent aerodynamic coefficients: **a** lift, **b** drag, **c** pitching moment, obtained from the URANS model (current work), LES model (Kim and Xie 2016), and experi-

ments (Lee and Gerontakos 2004) with oscillation cycle parameters $\alpha = 10^\circ + 15^\circ \sin(\omega t)$, $k_r = 0.05$

Table 5 Comparison of the dynamic stall and moment stall locations acquired from the HF and LF models from current work along with LES and experimental results for oscillation cycle parameters $\alpha = 10^\circ + 15^\circ \sin(\omega t)$, $k_r = 0.05$

Models	Moment stall (α_{ms}) (deg)	Dynamic stall (α_{ds}) (deg)
HF model (current work)	16.6	19.2
LF model (current work)	14.1	18.3
LES Kim and Xie (2016)	17.8	19.7
Experiments Lee and Gerontakos (2004)	17.5	21.1

can ideally be used in multifidelity methods as HF model and URANS as a LF model providing better alternatives in future design optimization studies.

4.5 Low-fidelity modeling

The LF model is an essential component of the multifidelity modeling method as the data obtained from the LF model are exploited to provide a global trend of the output response, which is then used to enhance the accuracy of HF approximation (Forrester et al. 2008; Kuya et al. 2011). The LF model estimates output response at a fraction of computational cost compared to the HF model but typically with lower accuracy. The LF model can be generated using various methods (Peherstorfer et al. 2018): (1) simplifying physics-based mathematical model (e.g., Euler inviscid method as LF and RANS as HF model), (2) changing the discretization of the physics-based model (e.g., coarser grid approximation, early stopping criteria), and (3) using a mathematical model as the LF model and experimental data as the HF model. In fluid dynamics problems, a popular way

of generating the LF model is by varying the discretization of the HF model (Giselle Fernández-Godino et al. 2019).

For this study, the LF model is generated by simplifying the HF CFD model by changing spatial and temporal discretization, and by selecting a convergence criteria such that the trend in the aerodynamic responses is preserved with the least possible computational time. In particular, the LF model is constructed with a grid with 157,000 cells, time-step of 0.015 sec, internal iteration of 1,000, and selecting Cauchy convergence criteria on the drag to 10^{-3} over 100 iterations. The constructed LF model reduces simulation time to approximately 1 h (wall-clock time) for a complete cycle with the baseline airfoil using 112 processor cores as the HF model.

Figure 6 shows the comparison of aerodynamic responses obtained from the LF model and HF model. Table 5 presents observed dynamic and moment stall angles for the HF and

LF model. The result shows only the upstroke part of the cycle, where DSV formation primarily affects airfoil aerodynamic response. The LF model shows a moderate resemblance with the HF model, where the LF model produces a very similar aerodynamic response up to $\alpha = 10^\circ$. The aerodynamic responses after $\alpha = 10^\circ$ are significantly different due to coarse spatial and temporal resolution. However, the LF model response still shows a similar trend as the HF model response.

5 Results

This section presents the results of the proposed optimization approach for mitigating dynamic stall over an airfoil. In the first subsection, the surrogate model construction and infill details are described. The following subsection

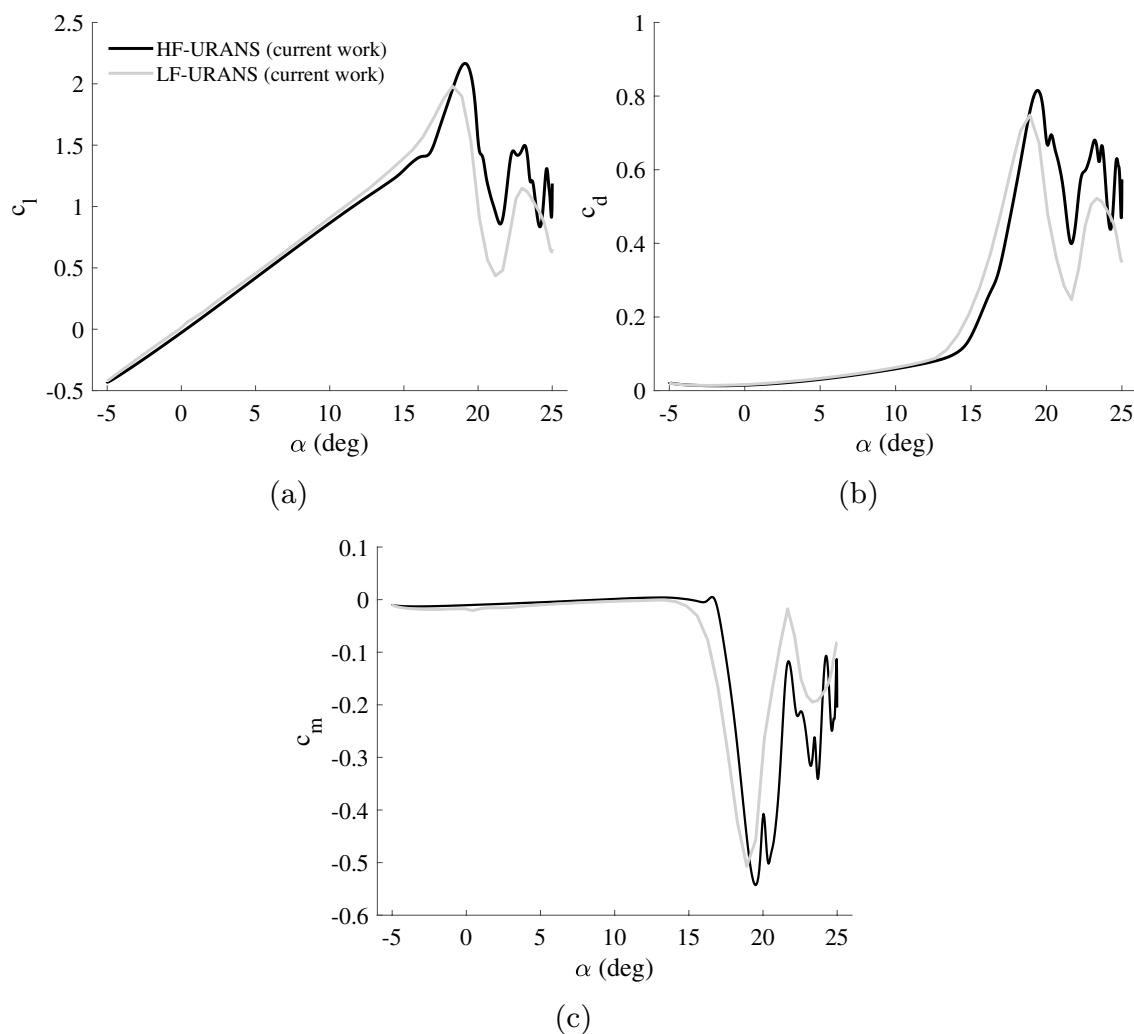


Fig. 6 Comparison of the time-dependent aerodynamic coefficients acquired from the high and low-fidelity simulation models: **a** lift, **b** drag, **c** pitching moment, results of the NACA 0012 airfoil with oscillation cycle parameters $\alpha = 10 + 15\sin(\omega t)$, $k = 0.05$ (results are shown only for the upstroke part of the cycle)

presents optimization results with CKR including the optimum design details and its dynamic stall characteristics.

5.1 Surrogate model construction

The proposed optimization algorithm is applied for mitigating dynamic stall over an airfoil. For this study, $\Delta\alpha = 3^\circ$ is selected in (4), which ensures that the optimum design produces at least 3° delay in dynamic stall angle over the baseline design.

The current optimization algorithm starts with generation of 20 HF samples and 220 LF samples using LHS method. The optimization algorithm has two parts: in the first part, the LF-KR model is generated with 220 LF samples and augmented sequentially with error-based infill strategy, until a saturated LF-KR model is produced. Two LF-KR models are developed, one for the objective function (LF-KR(f)) and another for the constraint function (LF-KR(g)). In every iteration, saturation condition of LF-KR(f) is checked using WMA of NRMSE metric as shown in Fig 7a. Figure 7b shows the NRMSE metric evolution of LF-KR(f) and LF-KR(g) surrogate over the error-based infill process. The first part of the algorithm terminates when NRMSE metric of LF-KR(f) plateaus (i.e., LF-KR is saturated), which is determined when $\text{NRMSE}_{WMA}^{(i)} - \text{NRMSE}_{WMA}^{(i-1)} \leq 10^{-5}$. The error-based infill process adds 38 infill samples to the initial LF sampling plan, resulting in a total of 258 LF samples.

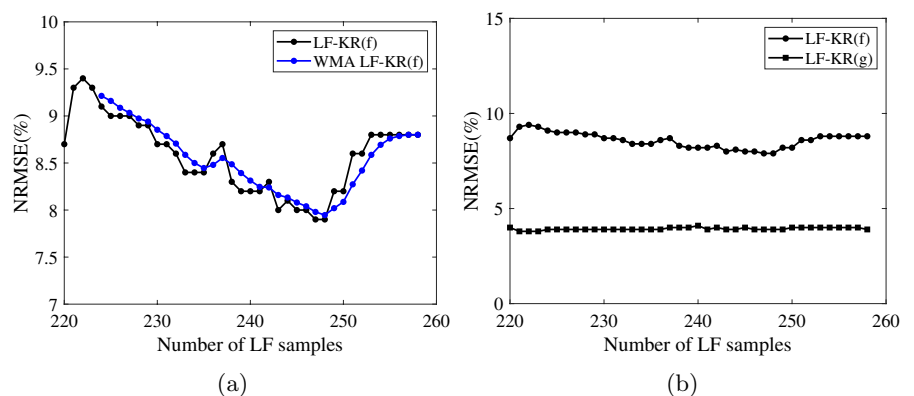
The first part of the algorithm aims to determine an appropriate LF sampling plan that captures the global trend in the objective function. In the second part of the optimization algorithm, 258 LF samples (obtained from the first part) and 20 HF samples are used to construct the initial CKR models for the HF objective function (CKR(f)) and the HF constraint function (CKR(g)). Further, the CKR models are refined using the EI-based infill approach on CKR(f) that provides balanced exploration–exploitation of the design space. In every iteration of the infill process, optimal designs are located using the constructed CKR models. A multi-start gradient-based optimizer is used to discover

optimal shape. In particular, the sequential least-square programming algorithm offered by the SciPy (Virtanen et al. 2019) python package is used with multi-start strategy of 200 samples, which are generated using the LHS plan to determine the optimal designs. The best result is realized as the optimal design. The EI-based infill process terminates with $\max(\mathbb{E}[I(\mathbf{x})])_{WMA} \leq 10^{-4}$ and the Euclidean distance between consecutive optimal designs $\|\mathbf{x}_{opt}^{(i)} - \mathbf{x}_{opt}^{(i-1)}\| \leq 0.002$. The optimal design variables (\mathbf{x}_{opt}) are normalized using min-max normalization before calculating the Euclidean norm. Such stringent termination conditions ensure accurate optimum with noisy data set. Figure 8a and b shows the progression of maximum EI magnitude and the Euclidean norm between consecutive optimal designs. The EI-based infill process terminates after adding 22 HF samples, making a total of 42 HF and 280 LF samples. Figure 8c and d shows the progression in optimal airfoil shapes and corresponding objective function magnitude in every infill iteration. The optimal shapes are numbered based on the number of HF samples used to construct CKR models. The optimal design acquired with 42 HF and 280 LF samples is considered as optimum airfoil shape (opt-42 in Fig. 8c) in the current study.

5.2 Optimal design

The grid and time independence study is performed on the optimum design to verify that the selected grid resolution and time-step size in HF CFD simulation model are still appropriate. A similar approach is taken as that for the baseline design mentioned in Sect. 4.3. Table 6 shows the results of the grid study on the optimized airfoil. The three grids with the highest spatial resolution show a minor variation in aerodynamic coefficients, with lift coefficient variation being $\Delta c_l < 0.003$ and drag coefficient variation under 4 d.c. Thus, considering the lowest simulation time requirement, the grid with 387,000 cells is still considered appropriate. Table 7 shows the time study results with the computation of average drag coefficient per cycle ($c_{d,avg}$). Richardson’s extrapolation

Fig. 7 Progression of the NRMSE metrics for the error-based infill process of the LF-KR model construction: **a** NRMSE and WMA NRMSE of LF-KR(f), and **b** NRMSE metric of LF-KR(f) and LF-KR(g)



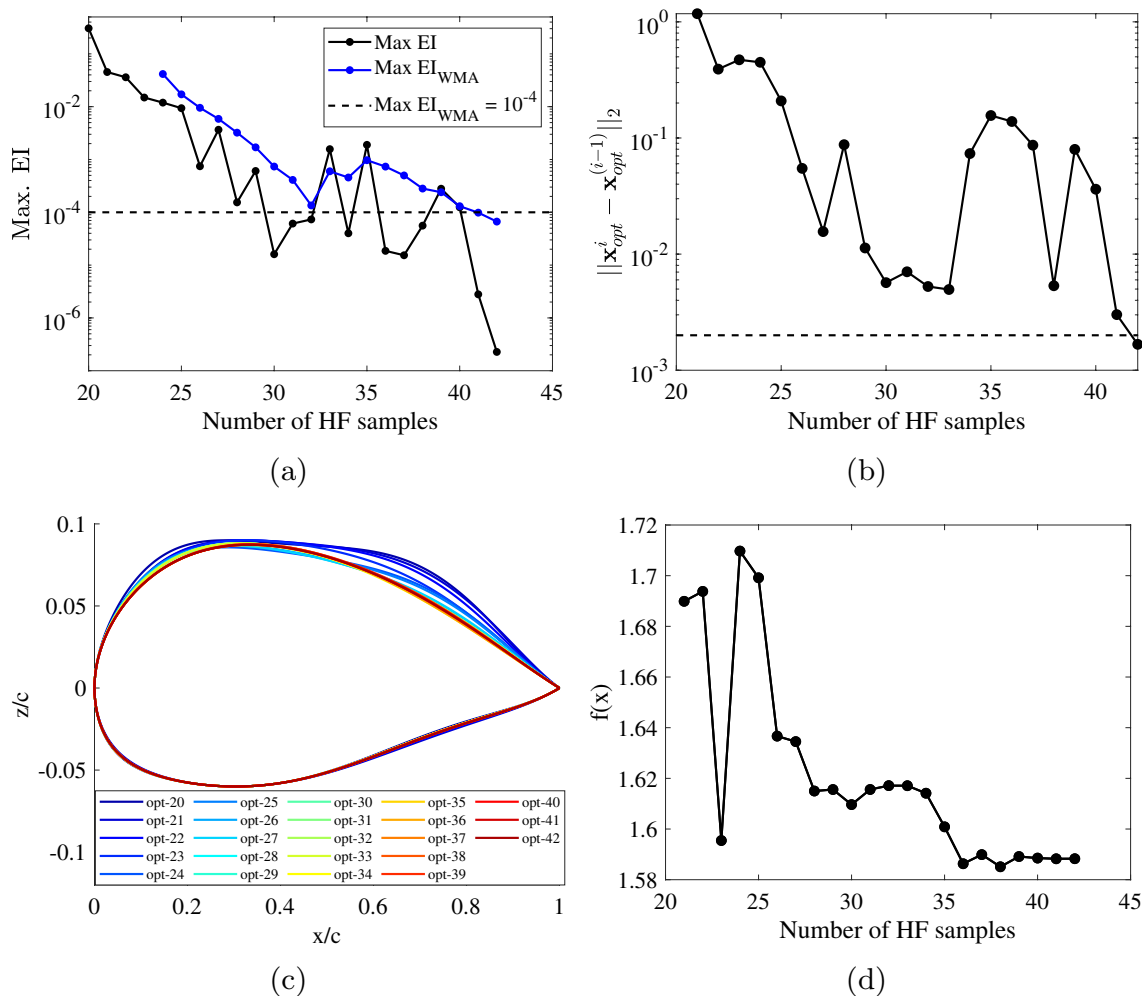


Fig. 8 Progression of metrics for the EI-based infill process with the CKR model: **a** maximum EI magnitude, **b** the Euclidean distance between consecutive optimum designs **c** the optimum shapes, and **d** objective function magnitude of optimum design

Table 6 Grid convergence study of the optimum design at $Re = 135,000$ and $\alpha = 4^\circ$

Grid	Number of elements	Lift	Drag (d.c.)	Simulation time* (min)
3	387,200	0.510	188	123
4	540,800	0.511	192	181
5	720,000	0.512	192	277

*Computed on a high-performance cluster with 112 processor cores. Wall-clock time

estimate of average drag coefficient per cycle is computed to be 1,703 d.c. The time-step of 0.0015 sec shows a reasonable agreement producing $c_{d_{err}} \leq 8$ d.c. From grid and time independence study of the optimal shape, the grid with 387,000 cells and a time-step of 0.0015 sec are still considered an appropriate selection for producing accurate HF simulation results.

Table 7 Results of the time-step independence study with the optimum design

dt (sec)	$c_{d_{avg}}$ (d.c./cycle)	Simulation time* (hrs/cycle)	$c_{d_{err}} = c_{d_{avg}} - c_{d_{RE}} $ (d.c.)
0.004	1,722	45	19.4
0.002	1,719	56	16.4
0.0015	1,710	62	7.4
0.0010	1,705	71	2.4

*Computed on a high-performance cluster with 112 processor cores. Wall-clock time

The optimum shape acquired with the CKR model is compared with the baseline design. Further, the optimum acquired from the current study is also compared with the optimal shape acquired from our previous study (Raul and Leifsson 2021), which uses KR model on HF data set for

the same problem formulation (Sect. 3.1) and it is denoted as ‘HF-KR’ model in this study. The HF-KR model is initialized with 60 HF samples generated with LHS plan and sequentially refined with EI-based infill approach and fixed budget of 20 infill samples.

Figure 9a shows the baseline and optimal designs obtained with the CKR and HF-KR models along with the region highlighting possible variations of airfoil shapes in the design space. In this study, optimum designs from the CKR and HF-KR models are denoted as Optimum-CKR and Optimum-HF-KR, respectively. The optimal shapes show significant variation from baseline with higher thickness, larger leading edge radius, and an aft camber than baseline. Table 8 presents the details of airfoil shapes for optimal and baseline designs. In particular, the optimal shapes from CKR and HF-KR models show a similar maximum thickness (t_{max}), whereas the location of a maximum thickness ($x_{t_{max}}$) is slightly different. The optimum-HF-KR shows higher maximum camber of 1.89% located at 62% of the chord. Similarly,

Table 8 Airfoil shape characteristics of the baseline and the optimum designs

Airfoil	t_{max}	$x_{t_{max}}$	m_{max}	$x_{m_{max}}$
Baseline	12	30	0	0
Optimum-HF-KR	14.6	35.3	1.89	62.0
Optimum-CKR	14.7	32.1	1.43	51.4

Shape properties are represented as percentage of the chord length

the Optimum-CKR has maximum camber of 1.43% located at 51.4% of the chord. Interestingly, both optimum shapes show an aft camber between 50 and 65% of chord length.

The optimal shapes are evaluated with the HF CFD simulation model over the upstroke pitching cycle, and their respective aerodynamic performance is compared against baseline and is presented in Fig. 9. The lift polar plot of optimal designs (see Fig. 9b) clearly shows a delay in the dynamic stall when compared with the baseline design.

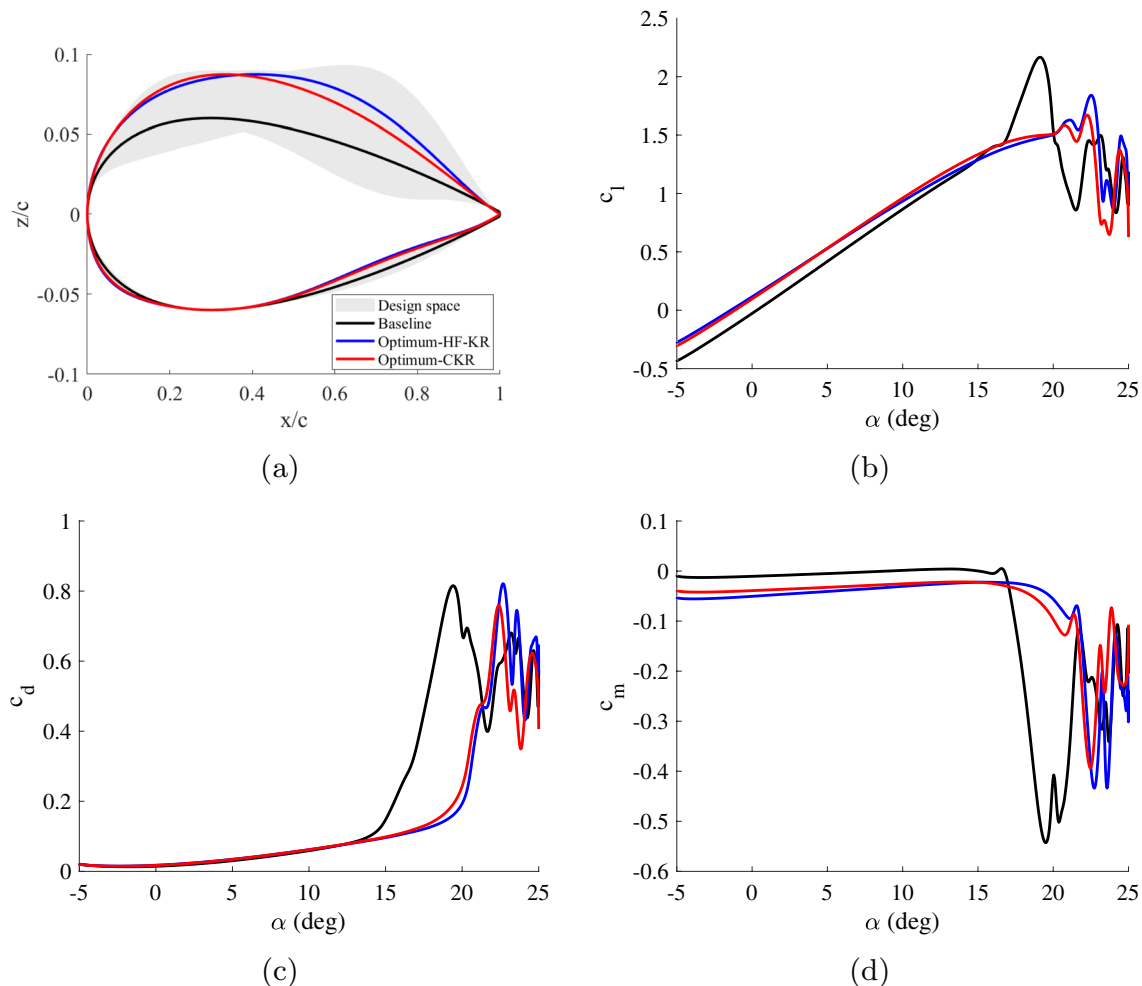


Fig. 9 Comparison of the shapes and aerodynamic loads of the baseline and optimum designs acquired from the HF-KR and CKR models: **a** airfoil shapes, **b** lift coefficient, **c** drag coefficient, and **d** pitching moment coefficient

Further, Fig. 9c and d shows the delay in the divergence of drag and pitching moment plots compared to baseline, which indicates the delay in the formation DSV. Table 9 provides essential details of dynamic stall characteristics for optimal and baseline designs along with their respective objective and constraint function values. Both the optimal designs delay the dynamic stall more than 3° as expected from problem formulation. The Optimum-HF-KR delays the dynamic stall to 22.5° , slightly higher than the Optimum-CKR. Both the optimal designs show similar characteristics of pitching moment polar plot and occurrence of moment stall (around 21.4°). The moment stall is recognized by a sudden drop in pitching moment magnitudes from Fig. 9d. Both optimal designs show a gradual reduction in pitching moments near moment stall angle followed by a sudden drop in pitching moment magnitude, which is a very different behavior compared to the baseline design. Further, peak magnitudes of lift, drag, and pitching moments are reduced for both optimal designs, with the Optimum-CKR showing the smallest peak magnitudes of aerodynamic coefficients.

Figure 10 presents streamlines and vorticity field around the baseline and optimal designs near the moment and dynamic stall angles for a better interpretation of results. It can be observed that near the baseline moment stall ($\alpha = 16.27^\circ$) and near dynamic stall ($\alpha = 18.91^\circ$) angles, baseline airfoil shows a formation and growth of DSV (Fig. 10 Baseline a and b), whereas the optimized airfoils do not show the formation of DSV at these angles. Instead, the optimal designs show a propagation of trailing edge flow reversal toward a leading edge as highlighted by streamlines (Figs. 10 Optimum-CKR, Optimum-HF-KR a, b). After the angle of attack of 19.2° , DSV separates from the baseline airfoil surface, causing a massive flow separation followed by formation and shedding of secondary vortices (Fig. 10 Baseline c and d). The trailing edge flow reversal continues to expand for the optimal designs until it reaches close to the leading edge. The DSV then forms, grows in size, and convects downstream (Fig. 10 Optimum-CKR, Optimum-HF-KR c and d).

The details of the dynamic stall mechanism in the upstroke pitching cycle can be analyzed by plotting skin friction coefficient (c_f) and negative coefficient of pressure ($-c_p$) over the suction side of airfoils. Figure 11 shows $-c_p$ and c_f as a function of angle of attack and chord location. The events shown in Figs. 9 and 10 can be identified here. As

the angle of attack increases, the suction peak near the leading edge increases, as seen from the hot-spots in Fig. 11a, c, and e. With the rise in suction peak, adverse pressure gradient increases, giving rise to the formation of separation bubble near the leading edge, seen by a scimitar-shaped blue region in Fig. 11b, d, and f. The baseline airfoil shows an early rise in suction peak and separation bubble formation at around $\alpha = 9^\circ$, while this process is delayed in both optimal designs. This is due to the larger leading edge radius of optimum airfoils that alleviate the increase in adverse pressure gradient during airfoil pitch up motion (Sharma and Visbal 2019). With further increase in the angle of attack, the separation bubble grows in size and propagates upstream. During the upstroke motion, airfoil trailing edge flow reversal also shows interesting behavior. As upstroke motion continues, flow starts to separate near trailing edge and travel upstream toward leading edge (seen in Fig. 11b, d, and f by blue dashed arrow). The trailing edge flow reversal is observed much early for optimal designs compared to baseline, mainly due to a higher thickness and aft camber. The Optimum-CKR shows a steady upstream movement of flow reversal point, whereas flow reversal moves gradually between $0^\circ \leq \alpha \leq 10^\circ$ (Fig. 11d) and then swiftly for the Optimum-HF-KR. This characteristic of the Optimum-HF-KR could be linked to the higher thickness and camber location on farther aft of an airfoil chord compared to the Optimum-CKR shape.

With further increase in the angle of attack, the formed separation bubble and flow reversal point move toward each other. The suction peak drop suddenly, followed by DSV formation, which occurs at around 15° for the baseline and around 20° for the optimal designs. On the baseline, DSV forms abruptly due to the bursting of the separation bubble, which can be classified as leading edge dynamic stall (Sharma and Visbal 2019). In case of optimal designs, DSV forms when trailing edge separation reaches separation bubble (Fig. 11d and f) and classified as trailing edge stall (Sharma and Visbal 2019). After the formation, DSV grows in size and travels downstream, which can be seen by the low pressure it generates over the airfoil surface (locus of hot-spots in $-c_p$ plots shown by black streak lines). It is observed that the DSV convects much faster over-optimized airfoils than the baseline (slope of black streak lines determines DSV speed of propagation). Additionally, it is also observed that DSV formed over optimal design leaves a weaker suction trail when compared to baseline, producing lower peak lift and pitching moment magnitudes in the case of the Optimum-CKR.

Overall, both optimal designs produce an almost similar delay in the dynamic stall angle compared to the baseline. Further, when objective and constraint function values are compared (Table 9), the Optimum-CKR shows a much lower objective function magnitude ($f(\mathbf{x}) = 1.59$) while closely

Table 9 Characteristics of the baseline and optimal shapes

Airfoil	α_{ds} (deg)	α_{ms} (deg)	$c_{l_{max}}$	$f(\mathbf{x})$	$g(\mathbf{x})$
Baseline (NACA 0012)	19.2	16.6	2.16	2	3
Optimum-HF-KR	22.5	21.5	1.84	1.78	-0.37
Optimum-CKR	22.3	n21.4	1.67	1.59	-0.11

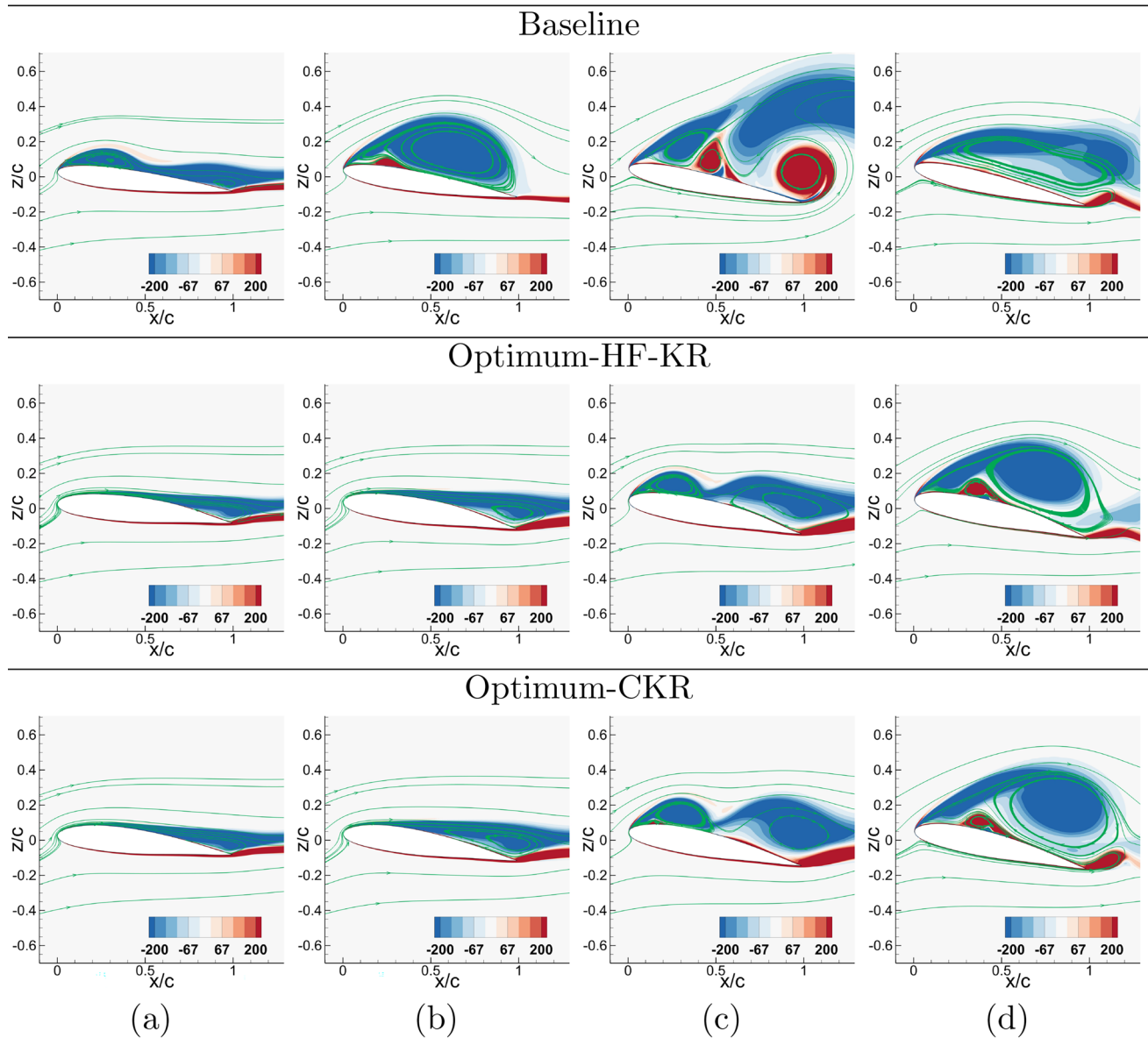


Fig. 10 Vorticity contour plot of the baseline and optimum airfoil shapes from the CKR and HF-KR models at **a** $\alpha = 16.27^\circ$, **b** $\alpha = 18.91^\circ$, **c** $\alpha = 21.66^\circ$, and **d** $\alpha = 22.56^\circ$

satisfying constraint ($g(\mathbf{x}) = -0.11$), thus producing the optimum design for the current problem formulation.

Table 10 shows the computational cost associated with using HF-KR and CKR surrogate models for the current optimization problem. The major cost of computation comes from running CFD simulations, whereas cost of executing optimization algorithm is comparatively negligible. For this study, SuperMicro servers each with two 2.6 GHz 8-Core Intel Haswell processors (Intel E5-2640 v3) are used. In general, each HF CFD evaluation takes approximately 4,480 CPU hours (computed on high-performance cluster with processor cores), whereas each LF CFD evaluation takes approximately 112 CPU hours (computed on high-performance cluster with

112 processor cores). The entire optimization with the HF-KR model utilizes a total of 80 HF samples taking approximately 358,400 CPU hours. Similarly, optimization with the CKR model takes 42 HF samples and 280 LF samples consuming approximately 219,520 CPU hours, producing almost 39% in computational cost-saving than HF-KR.

6 Conclusion

This paper proposes the use of a multifidelity modeling technique to passively mitigate dynamic stall characteristics of an airfoil through aerodynamic shape optimization (ASO).

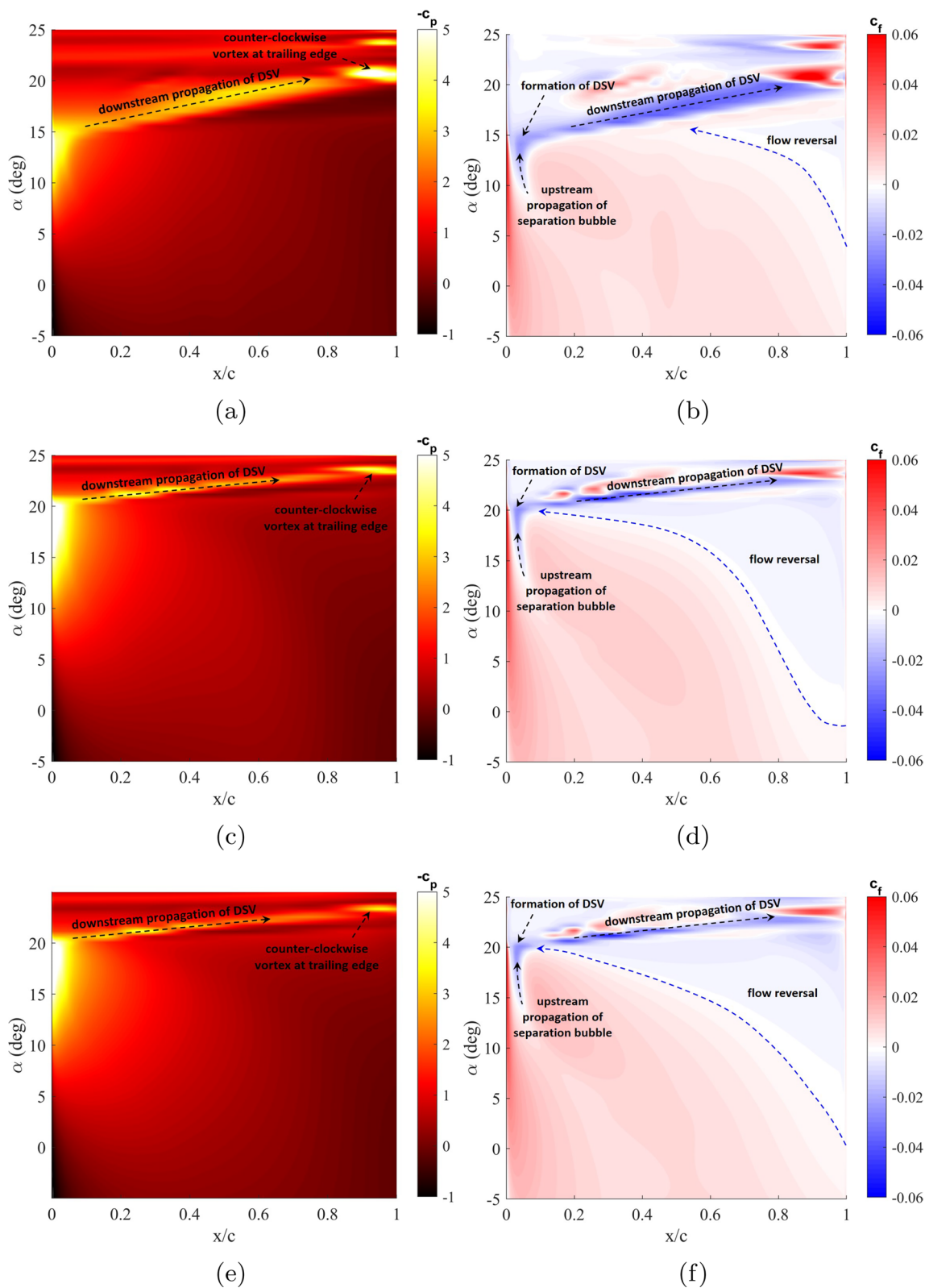


Fig. 11 Contours of the negative pressure coefficient ($-c_p$) and the skin friction coefficient (c_f) over the upper surface of the airfoils: the baseline (a, b), Optimum-HF-KR (c, d), and Optimum-CKR (e, f)

Table 10 Computational cost of the surrogate modeling

Surrogate model	HF samples	LF samples	CPU hours*	Cost savings
HF-KR	80	–	358,400	
CKR	42	280	219,520	38.7%

*Computed using average HF simulation time of 40 h and average LF simulation time of 1 h on a high-performance cluster with 112 processor cores. Wall-clock time

In particular, the Cokriging regression (CKR) multifidelity model, which can filter noisy data, is used along with an unsteady computational fluid dynamics (CFD) model to construct approximations of the objective and constraint functions in the ASO problem formulation. The CKR model is efficiently constructed with a conservative number of HF samples and a large number of low-fidelity samples and adaptively enhanced with infill strategies, keeping the overall computational cost low. The CKR model is utilized with a multi-start gradient optimizer to find the optimum airfoil shape.

The optimal airfoil shape found by the proposed approach has a larger leading edge radius, higher thickness, and an increased aft camber when compared to the baseline airfoil. Post-optimality analysis showed that the optimum design significantly delays the DSV formation with reduced peak lift, drag, and pitching moment magnitudes. Further, it was observed that the DSV formation over the optimized shape produces a much weaker suction trail and convects faster downstream when compared to the baseline.

The performance of the optimized shape from the CKR model is also compared with the optimum design acquired using a high-fidelity Kriging regression (HF-KR) model. Overall, both optimum designs produce a similar delay in the dynamic stall angle; however, when the objective and constraint function magnitudes are compared, the optimum from the CKR model provides a better design for the current problem formulation. Further, the multifidelity CKR model requires roughly 39% less time to obtain the optimum design compared to a single-fidelity surrogate using the HF-KR model.

The proposed multifidelity modeling approach using CKR and infill criteria has been demonstrated to efficiently yield optimal airfoil shapes for dynamic stall mitigation at a low computational cost. Although the approach was applied to a general airfoil under the dynamic stall, the proposed approach can be extended to other aerospace systems, including helicopter rotors, aircraft, unmanned air vehicles, wind turbines, and compressor blades. The proposed approach will be applied to determine robust design under uncertainty of the airfoil oscillating motion parameters in future work. Such an investigation could lead to an improved understanding of the effect of uncertainty in the motion

parameters on the airfoil dynamic stall and mitigation of its adverse characteristics.

Acknowledgements This material is based upon work supported by the National Science Foundation under Award No. 1739551.

Declarations

Conflict of interest On behalf of all authors, the corresponding author states that there is no conflict of interest.

Replication of results The paper contains sufficient details that is needed to replicate the results with limitations due to the heuristic nature of the optimization algorithm and infill process. The code and data of this study will be made available by request.

References

- Abbott S (2001) Understanding analysis. Springer, New York
- Bailly J, Bailly D (2019) Multifidelity aerodynamic optimization of a helicopter rotor blade. *AIAA J* 57(8):3132–3144
- Blatman G. (2009) Adaptive sparse polynomial chaos expansions for uncertainty propagation and sensitivity analysis. PhD thesis, Université Blaise Pascal, Clermont-Ferrand (2009). Doctoral thesis supervised by Sudret, Bruno Mechanical engineering Clermont-Ferrand 2 2009. <http://www.theses.fr/2009CLF21955>
- Brandon JM (1991) Dynamic stall effects and applications to high performance aircraft. Technical Report AGARD-R-776, Special course on aircraft dynamics at high angles of attack: experiments and modelling, NASA Langley Research Center
- Buchner A, Lohry M, Martinelli L, Soria J, Smits A (2015) Dynamic stall in vertical axis wind turbines: comparing experiments and computations. *J Wind Eng Ind Aerodyn* 146:163–171
- Carr LW, McAlister KW, McCroskey WJ (1977) Analysis of the development of dynamic stall based on oscillating airfoil experiments. NASA Technical Note NASA TN D-8382
- Carr LW (1988) Progress in analysis and prediction of dynamic stall. *J Aircr* 25(1):6–17
- Chandrasekhara M, Martin PB, Tung C (2004) Compressible dynamic stall control using a variable droop leading edge airfoil. *J Aircr* 41(4):862–869
- Daróczy L, Janiga G, Petrasch K, Webner M, Thévenin D (2015) Comparative analysis of turbulence models for the aerodynamic simulation of h-darrieus rotors. *Energy* 90:680–690
- De Giorgi MG, Motta V, Suma A (2020) Influence of actuation parameters of multi-dbd plasma actuators on the static and dynamic behaviour of an airfoil in unsteady flow. *Aerosp Sci Technol* 96:105587. <https://doi.org/10.1016/j.ast.2019.105587>
- Echeverría D, Hemker P (2008) Manifold mapping: a two-level optimization technique. *Comput Vis Sci* 11(4–6):193–206
- Echeverría D, et al. (2007) Multi-level optimization. space mapping and manifold mapping. PhD thesis, Universiteit van Amsterdam, Amsterdam, The Netherlands. Research conducted at: Centrum voor Wiskunde en Informatica. <https://hdl.handle.net/11245/1.270966>
- Economon TD, Palacios F, Copeland SR, Lukaczyk TW, Alonso JJ (2016) Su2: an open-source suite for multiphysics simulation and design. *AIAA J* 54(3):828–846
- Economon T, Palacios F, Alonso J (2013) Unsteady aerodynamic design on unstructured meshes with sliding interfaces. In: 51st AIAA aerospace sciences meeting including the new horizons forum and aerospace exposition, p. 632 (Grapevine (Dallas/Ft.

- Worth Region), Texas, 07-10 January 2013). <https://doi.org/10.2514/6.2013-632>
- Ellington CP (1999) The novel aerodynamics of insect flight: applications to micro-air vehicles. *J Exp Biol* 202(23):3439–3448
- Forrester AI, Keane AJ (2009) Recent advances in surrogate-based optimization. *Prog Aerosp Sci* 45(1–3):50–79
- Forrester J, Keane AI, Bressloff AJ (2006) Design and analysis of “Noisy” computer experiments. *AIAA J* 44(10):2331–2339
- Forrester AI, Sobester A, Keane AJ (2007) Multi-fidelity optimization via surrogate modelling. *Proc R Soc A: Math, Phys Eng Sci* 463(2088):3251–3269
- Forrester AI, Sobester A, Keane AJ (2007) Multi-fidelity optimization via surrogate modelling. *Proc R Soc A: Math, Phys Eng Sci* 463(2088):3251–3269. <https://doi.org/10.1098/rspa.2007.1900>
- Forrester A, Sobester A, Keane A (2008) Engineering design via surrogate modelling: a practical guide. John Wiley & Sons Ltd, Chichester
- Giselle Fernández-Godino M, Park C, Kim NH, Haftka RT (2019) Issues in deciding whether to use multifidelity surrogates. *AIAA J* 57(5):2039–2054
- Gu L, Yang R (2006) On reliability-based optimisation methods for automotive structures. *Int J Mater Prod Technol* 25(1–3):3–26
- Hand B, Kelly G, Cashman A (2017) Numerical simulation of a vertical axis wind turbine airfoil experiencing dynamic stall at high Reynolds numbers. *Comput Fluids* 149:12–30
- Harris FD, Prunyn RR (1968) Blade stall half fact, half fiction. *J Am Helicopter Soc* 13(2):27–48
- Jameson A (2003) Aerodynamic shape optimization using the adjoint method. Lectures at the Von Karman Institute, Brussels
- Kim Y, Xie Z-T (2016) Modelling the effect of freestream turbulence on dynamic stall of wind turbine blades. *Comput Fluids* 129:53–66
- Koziel S, Yang XS (2011) *Studies in computational intelligence*. Springer, Berlin Heidelberg
- Koziel S, Bandler JW, Madsen K (2008) Quality assessment of coarse models and surrogates for space mapping optimization. *Optim Eng* 9(4):375–391
- Koziel S, Cheng QS, Bandler JW (2008) Space mapping. *IEEE Microw Mag* 9(6):105–122
- Kumar D, Cesnik CE (2015) Performance enhancement in dynamic stall condition using active camber deformation. *J Am Helicopter Soc* 60(2):1–12
- Kuya Y, Takeda K, Zhang X, Forrester AI (2011) Multifidelity surrogate modeling of experimental and computational aerodynamic data sets. *AIAA J* 49(2):289–298
- Laurenceau J, Meaux M (2008) Comparison of gradient and response surface based optimization frameworks using adjoint method. In: 49th AIAA/ASME/ASCE/AHS/ASC Structures, Structural Dynamics, and Materials Conference, 16th AIAA/ASME/AHS Adaptive Structures Conference, 10th AIAA Non-Deterministic Approaches Conference, 9th AIAA Gossamer Spacecraft Forum, 4th AIAA Multidisciplinary Design Optimization Specialists Conference, p. 1889 (Schaumburg, IL, 10th April 2008)
- Lee T, Gerontakos P (2004) Investigation of flow over an oscillating airfoil. *J Fluid Mech* 512:313–341
- Lee T, Gerontakos P (2006) Dynamic stall flow control via a trailing-edge flap. *AIAA J* 44(3):469–480
- Leifsson L, Koziel S (2015) *Simulation-driven aerodynamic design using variable-fidelity models*. Imperial College Press, London, UK
- Mani K, Lockwood BA, Mavriplis DJ (2012) Adjoint-based unsteady airfoil design optimization with application to dynamic stall. *Am Helicopter Soc* 3:1940
- McCroskey WJ, Carr LW, McAlister KW (1976) Dynamic stall experiments on oscillating airfoils. *AIAA J* 14(1):57–63
- McCroskey WJ, McAlister K, Carr L, Pucci S, Lambert O, Indergrand R (1981) Dynamic stall on advanced airfoil sections. *J Am Helicopter Soc* 26(3):40–50
- McKay MD, Beckman RJ, Conover WJ (2000) A comparison of three methods for selecting values of input variables in the analysis of output from a computer code. *Technometrics* 42(1):55–61
- Menter FR (1994) Two-equation eddy-viscosity turbulence models for engineering applications. *AIAA J* 32(8):1598–1605
- Müller-Vahl HF, Nayeri CN, Paschereit CO, Greenblatt D (2016) Dynamic stall control via adaptive blowing. *Renew Energy* 97:47–64
- Nadarajah SK, Jameson A (2007) Optimum shape design for unsteady flows with time-accurate continuous and discrete adjoint method. *AIAA J* 45(7):1478–1491
- Nagawkar J, Ren J, Du X, Leifsson L, Koziel S (2021) Single- and multipoint aerodynamic shape optimization using multifidelity models and manifold mapping. *J Aircr* 58:1–18
- Niu J, Lei J, Lu T (2018) Numerical research on the effect of variable droop leading-edge on oscillating naca 0012 airfoil dynamic stall. *Aerosp Sci Technol* 72:476–485
- OpenFOAM - The open source computational fluid dynamics (CFD) Toolbox. <http://openfoam.com> ((2021/09/27))
- Palacios F, Alonso J, Duraisamy K, Colonno M, Hicken J, Aranake A, Campos A, Copeland S, Economon T, Lonkar A, et al (2013) Stanford university unstructured (su 2): an open-source integrated computational environment for multi-physics simulation and design. In: 51st AIAA aerospace sciences meeting including the new horizons forum and aerospace exposition, Grapevine (Dallas/Ft. Worth Region), Texas, p. 287 (7-10 January 2013)
- Palacios F, Economon TD, Aranake A, Copeland SR, Lonkar AK, Lukaczyk TW, Manosalvas DE, Naik KR, Padron S, Tracey B, et al (2014) Stanford university unstructured (su2): Analysis and design technology for turbulent flows. In: 52nd aerospace sciences meeting, National Harbor, Maryland, p. 0243 (13–17 January)
- Peherstorfer B, Willcox K, Gunzburger M (2018) Survey of multifidelity methods in uncertainty propagation, inference, and optimization. *SIAM Rev* 60(3):550–591
- Peri D, Tinti F (2012) A multistart gradient-based algorithm with surrogate model for global optimization. *Comm Appl Ind Math*. <https://doi.org/10.1685/journal.caim.393>
- Raul VV, Leifsson LT (2021) Aerodynamic shape optimization for delaying dynamic stall of airfoils using cokriging regression. In: AIAA Scitech 2021 Forum, p. 0340
- Raul V, Leifsson L (2021) Surrogate-based aerodynamic shape optimization for delaying airfoil dynamic stall using kriging regression and infill criteria. *Aerosp Sci Technol* 111:106555. <https://doi.org/10.1016/j.ast.2021.106555>
- Rogalsky T, Derksen R (2009) Bézier-params parameterization for airfoil optimization. *Can Aeronaut Space J* 55(3):163–174
- Roy CJ (2003) Grid convergence error analysis for mixed-order numerical schemes. *AIAA J* 41(4):595–604
- Sharma A, Visbal M (2019) Numerical investigation of the effect of airfoil thickness on onset of dynamic stall. *J Fluid Mech* 870:870–900. <https://doi.org/10.1017/jfm.2019.235>
- Shi L, Yang R, Zhu P (2012) A method for selecting surrogate models in crashworthiness optimization. *Struct Multidisc Optim* 46(2):159–170
- Simpson TW, Poplinski J, Koch PN, Allen JK (2001) Metamodels for computer-based engineering design: survey and recommendations. *Eng Comput* 17(2):129–150
- Sjögren R, Svensson D (2021) pyDOE2: an experimental design package for python. Available at <https://pypi.org/project/pyDOE2/> ((2021/09/27))
- Sobieczky H (1999) *Parametric airfoils and wings. Recent development of aerodynamic design methodologies*. Vieweg + Teubner Verlag, Wiesbaden, pp 71–87

- Tang J, Hu Y, Song B, Yang H (2017) Unsteady aerodynamic optimization of airfoil for cycloidal propellers based on surrogate model. *J Aircr* 54(4):1241–1256
- Thelen AS, Leifsson LT, Beran PS (2020) Multifidelity flutter prediction using regression cokriging with adaptive sampling. *J Fluids Struct* 97:103081
- Thelen A, Leifsson L, Beran P (2020) Aeroelastic flutter prediction using multifidelity modeling of the generalized aerodynamic influence coefficients. *AIAA J* 58(11):4764–4780
- Veerakumar R, Raul V, Liu Y, Wang X, Leifsson L, Hu H (2020) Meta-modeling-based parametric optimization of dbd plasma actuation to suppress flow separation over a wind turbine airfoil model. *Acta Mech Sin* 36(2):260–274
- Virtanen P, Gommers R, Oliphant TE, Haberland M, Reddy T, Cournapeau D, Burovski E, Peterson P, Weckesser W, Bright J, et al. (2019) Scipy 1.0—fundamental algorithms for scientific computing in python. arXiv preprint [arXiv:1907.10121](https://arxiv.org/abs/1907.10121)
- Vu NA, Lee JW (2015) Aerodynamic design optimization of helicopter rotor blades including airfoil shape for forward flight. *Aerosp Sci Technol* 42:106–117. <https://doi.org/10.1016/j.ast.2014.10.020>
- Wang Q, Zhao Q (2018) Rotor airfoil profile optimization for alleviating dynamic stall characteristics. *Aerosp Sci Technol* 72:502–515
- Wang Q, Zhao Q (2020) Rotor blade aerodynamic shape optimization based on high-efficient optimization method. *Proc Inst Mech Eng, Part G: J Aerosp Eng* 234(2):375–387
- Wang S, Ingham DB, Ma L, Pourkashanian M, Tao Z (2010) Numerical investigations on dynamic stall of low Reynolds number flow around oscillating airfoils. *Comput Fluids* 39(9):1529–1541
- Wang Q, Zhao Q, Wu Q (2015) Aerodynamic shape optimization for alleviating dynamic stall characteristics of helicopter rotor airfoil. *Chin J Aeronaut* 28(2):346–356
- Wong T, Malley O, Brien D, (2006) Investigation of effect of dynamic stall and its alleviation on helicopter performance and loads. *Annu Forum Proc-Am Helicopter Soc* 62–3:1749
- Yamazaki W, Arakawa Y (2016) Numerical/experimental investigation of airfoil shape for small vawt. 34th Wind energy symposium. American Institute of Aeronautics and Astronautics, Inc., San Diego, p 1733
- Yu YH, Lee S, McAlister KW, Tung C, Wang CM (1995) Dynamic stall control for advanced rotorcraft application. *AIAA J* 33(2):289–295
- Zhou Z, Ong YS, Nguyen MH, Lim D (2005) A study on polynomial regression and gaussian process global surrogate model in hierarchical surrogate-assisted evolutionary algorithm. *IEEE Congress Evol Comput* 3:2832–2839
- Zhu H, Hao W, Li C, Ding Q, Wu B (2019) Application of flow control strategy of blowing, synthetic and plasma jet actuators in vertical axis wind turbines. *Aerosp Sci Technol* 88:468–480. <https://doi.org/10.1016/j.ast.2019.03.022>

Publisher's Note Springer Nature remains neutral with regard to jurisdictional claims in published maps and institutional affiliations.

Springer Nature or its licensor (e.g. a society or other partner) holds exclusive rights to this article under a publishing agreement with the author(s) or other rightsholder(s); author self-archiving of the accepted manuscript version of this article is solely governed by the terms of such publishing agreement and applicable law.